Geochemistry, Geophysics, Geosystems

RESEARCH ARTICLE
10.1029/2020GC009322

Extreme Heterogeneity in Mid-Ocean Ridge Mantle Revealed in Lavas From the 8°20′N Near-Axis Seamount Chain

Molly Anderson[1,2], V. Dorsey Wanless[1], Michael Perfit[2], Ethan Conrad[2], Patricia Gregg[3], Daniel Fornari[4], and W. Ian Ridley[5]

[1]Department of Geosciences, Boise State University, Boise, ID, USA, [2]Department of Geological Sciences, University of Florida, Gainesville, FL, USA, [3]University of Illinois at Urbana-Champaign, Champaign, IL, USA, [4]Department of Geology and Geophysics, Woods Hole Oceanographic Institution, Woods Hole, MA, USA, [5]United States Geological Survey, Denver, CO, USA

Key Points:

- Geochemistry of near-axis seamounts reveals extreme heterogeneity in the sub-ridge East Pacific Rise mantle
- Heterogeneous mantle is preserved within 22 km of the ridge, and on individual seamounts
- Variations in the seamount lava compositions are explained by melting a heterogeneous mantle to variable degrees

Supporting Information:

- Supporting Information S1
- Supplement 3
- Table S1
- Table S2
- Table S3

Correspondence to:
M. Anderson,
mollyanderson@ufl.edu

Citation:
Anderson, M., Wanless, V. D., Perfit, M., Conrad, E., Gregg, P., Fornari, D., & Ridley, W. I. (2021). Extreme mantle heterogeneity in mid-ocean ridge mantle revealed in lavas from the 8°20′N near-axis seamount chain. *Geochemistry, Geophysics, Geosystems*, *22*, e2020GC009322. https://doi.org/10.1029/2020GC009322

Received 31 JUL 2020
Accepted 5 DEC 2020
Corrected 18 MAR 2021

This article was corrected on 18 MAR 2021. See the end of the full text for details.

Abstract Lavas that have erupted at near-axis seamounts provide windows into mid-ocean ridge mantle heterogeneity and melting systematics which are not easily observed on-axis at fast-spreading centers. Beneath ridges, most heterogeneity is obscured as magmas aggregate toward the ridge, where they efficiently mix and homogenize during transit and within shallow magma chambers prior to eruption. To understand the deeper magmatic processes contributing to oceanic crustal formation, we examine the compositions of lavas erupted along a chain of near-axis seamounts and volcanic ridges perpendicular to the East Pacific Rise. We assess the chemistry of near-ridge mantle using a ~200 km-long chain at ~8°20′N. High-resolution bathymetric maps are used with geochemical analyses of ~300 basalts to evaluate the petrogenesis of lavas and the heterogeneity of mantle feeding these near-axis eruptions. Major and trace element concentrations and radiogenic isotope ratios are highly variable on <1 km scales, and reveal a continuum of depleted, normal, and enriched basalts spanning the full range of ridge and seamount compositions in the northeast Pacific. There is no systematic compositional variability along the chain. Modeling suggests that depleted mid-ocean ridge basalt (DMORB) lavas are produced by ~5%–15% melting of a depleted mid-ocean ridge (MOR) mantle. Normal mid-ocean ridge basalts (NMORB) form from 5% to 15% melting of a slightly enriched MOR mantle. Enriched mid-ocean ridge basalts (EMORB) range from <1% melting of 10% enriched mantle to >15% melting of 100% enriched mantle. The presence of all three lava types along the seamount chain, and on a single seamount closest to the ridge axis, confirms that the sub-ridge mantle is much more heterogeneous than is commonly observed on-axis and heterogeneity exists over small spatial scales.

Plain Language Summary Basalts erupted from submarine volcanoes (seamounts) near mid-ocean ridges can provide key information about the composition and dynamics of Earth's upper mantle. However, no existing studies examine long chains of seamounts built on the flanks of spreading ridges like the East Pacific Rise as presented here. We measured major and trace element abundances in conjunction with radiogenic isotope ratios to determine the source and origins of lavas from 8°20′N seamounts. Our geochemical investigation of the seamount chain provides us with an opportunity to determine the range of compositions of the mantle beneath a mid-ocean ridge, their distribution in the mantle, and how and to what degree the mantle melts beneath these seamounts. We analyzed the composition of about 300 rocks from the seamounts and found that the lava compositions on this single chain compare well with the compositions of lavas erupted along the northern East Pacific Rise and from many seamounts scattered about on the northeastern Pacific oceanic crust. We find that this chain is extremely geochemically variable even within 22 km of the ridge axis on the scale of a few kilometers due to different amounts of mixing and melting of a heterogeneous mantle.

1. Introduction

Understanding how and where magmas are generated, transported, and focused in the mantle before erupting at mid-ocean ridges (MORs) and seamounts is fundamental to determining how the majority of the Earth's oceanic crust is formed. Most investigations of mid-ocean ridge basalt (MORB) geochemistry occur

on-axis, as a means of determining the nature and evolution of upper mantle source heterogeneities, melting processes, and melt differentiation in the crust. Significantly fewer detailed surveys focus on transform faults, individual seamounts, and abyssal hills (Allan & Batiza, 1987; Batiza & Vanko, 1984; Batiza et al., 1990; Clague et al., 2000; Coumans et al., 2015; A. S. Davis & Clague, 2000; Fornari et al., 1988a, 1988b; Gill et al., 2016; Macdonald et al., 1992; Niu & Batiza, 1997; Niu et al., 2002; Perfit & Chadwick, ; Perfit et al., 1996; Pockalny et al., 1997; Reynolds & Langmuir, 2000; Sun et al., 2020).

MOR magmas form by decompression melting as the Earth's mantle upwells beneath the MOR axis (Carmichael et al., 1974; Key et al., 2013; Langmuir et al., 1992; Mckenzie & Bickle, 1988). Normal mid-ocean ridge basalts (NMORB), which are the dominant composition erupted at fast-spreading ridges, form by differentiation and homogenization of a range of primitive melt compositions produced from variable extents of melting beneath MORs. This results in relatively limited compositional variability (Batiza & Niu, 1992; Perfit et al., 1994; Rubin & Sinton, 2007; Stracke & Bourdon, 2009). Traditional models of melt generation and transport beneath MORs propose that the onset of fractional melting occurs at a relatively constant depth beneath a given ridge and extent of melting increases with the height of the melting column. Modeling has suggested that the region of melting is ~100–200 km wide at its base (e.g., Forsyth et al., 1998; Langmuir et al., 1992; Phipps-Morgan, 1987) and melting ceases when the upwelling mantle intersects the base of the lithosphere (Hebert & Montési, 2010; Niu, 1997; Niu et al., 1996). This results in higher total extents of melting directly beneath the ridge axis and decreasing extents of melting off-axis with increasing lithospheric thickness, resulting in a roughly triangular-shaped melting region (Batiza et al., 1990; Langmuir et al., 1992; O'Hara, 1985; Plank & Langmuir, 1992). Magmas generated across the melting region ascend through the mantle until they intersect a permeability barrier at the base of the lithosphere, are focused laterally upslope toward the ridge axis (Phipps-Morgan, 1987; Sparks & Parmentier, 1991; Spiegelman & McKenzie, 1987), and are eventually pooled in axial magma chambers. As a result, the range of geochemical signatures may be obscured in lavas erupted on-axis, as these melts are aggregated during ascent and focused in the mantle beneath the axis (P. M. Gregg et al., 2012; Hebert & Montési, 2010; Katz, 2008; Keller et al., 2017; Niu et al., 2002; Phipps-Morgan, 1987; Spiegelman & McKenzie, 1987) and further homogenized in shallow crustal melt lenses (e.g., Perfit & Chadwick, ; Rubin et al., 2009; Sinton & Detrick, 1992). While shallow magma chambers may promote moderate fractional crystallization, homogenization results in a relatively limited range of trace element and isotopic compositions in lavas erupted on-axis at fast-spreading MORs (Perfit & Chadwick, ; Perfit et al., 1994; Rubin & Sinton, 2007; Sinton & Detrick, 1992; V. D. Wanless & Shaw, 2012).

The rarer eruption of enriched mid-ocean ridge basalts (EMORB) (Batiza & Niu, 1992; Perfit et al., 1994; Reynolds et al., 1992; C. L. Waters et al., 2011) and1 highly depleted mid-ocean ridge basalts (DMORB) suggests that homogenization is not always efficient and indicates a range of melt compositions can be produced in the sub-ridge mantle (Allan & Batiza, 1987; Brandl et al., 2012; Gale et al. 2013; Katz & Weatherley, 2012; Lundstrom et al., 1999; Mallick et al., 2019; Niu & Batiza, 1997a, 1997b; Niu et al., 2002; Perfit et al., 1996; Sims et al., 2002; M. C. Smith et al., 2001; C. L. Waters et al., 2011; Zindler et al., 1984). Unfortunately, even the less abundant E- and DMORB are likely influenced by magma homogenization to some extent, and thus the compositional range of primitive melts produced in the sub-ridge mantle is not well constrained by investigations of on-axis lavas.

Off-axis volcanic features, such as ridge flanks and seamounts, are alternative windows into the upper mantle due to the absence of steady-state magma chambers (Batiza & Niu, 1992; Perfit & Chadwick,). Studies of lavas erupted at near-ridge (5–30 km) and off-axis seamounts reveal greater compositional variability compared to lavas erupted on-axis (Allan et al., 1989; Clague et al., 2000; Coumans et al., 2015; A. S. Davis & Clague, 2000; Fornari et al., 1988; Gill et al., 2016; Scheirer & Macdonald, 1995). For example, some individual seamounts and short seamount chains in the northeastern Pacific are comprised of lavas that range from DMORB to highly enriched EMORB, with significant compositional variations observed on small (<5 km) scales and in greater abundance than is found on-axis (Allan & Batiza, 1987; Batiza et al., 1989, 1990; Brandl et al., 2012; Gill et al., 2016; Niu & Batiza, 1997a, 1997b; Niu et al., 2002; Shimizu et al., 2016; Zindler et al., 1984). These studies indicate that near-ridge seamount volcanism is commonly sourced from the mantle that supplies the MOR axis, but seamounts preserve a wider range of primary melts (Batiza & Niu, 1992; Perfit & Chadwick,).

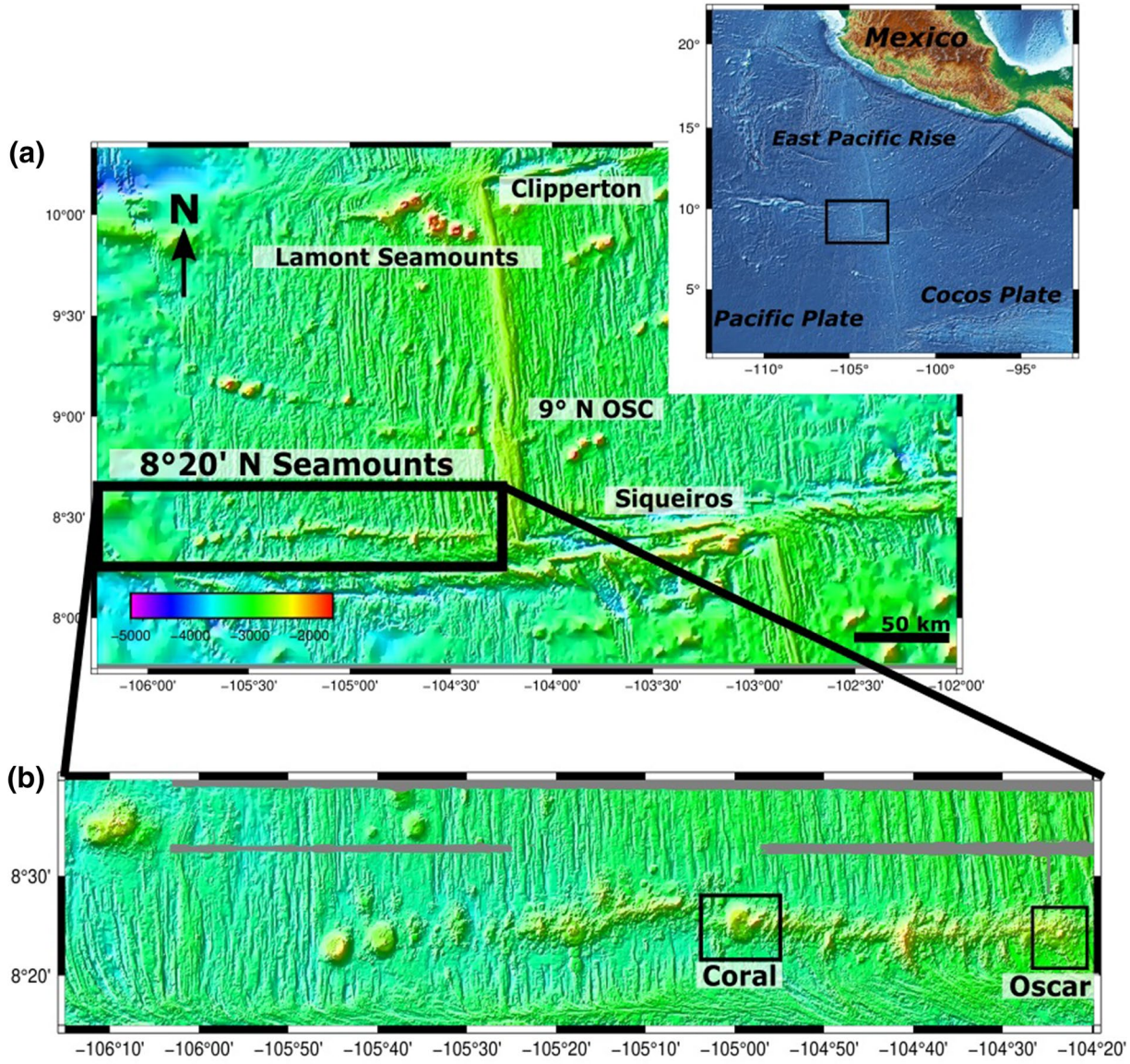

Figure 1. Location and morphology of the 8°20′N seamount chain. (a) SeaSat 1-km gridded satellite altimetry data for the northeastern Pacific between the Clipperton and Siqueiros transform faults (S. M. Carbotte et al., 2004) that bound the first-order segment of the East Pacific Rise (EPR). Location of AT37-05 EM122 multibeam bathymetry over the 8°20′N seamount chain, gridded at 70-m node spacing shown in (b). (b) New MR1 bathymetry displays key morphostructural features including well-defined ~ N-S lineated abyssal hill fabric north of the seamount chain. The southern area of the eastern half of the seamount chain includes curvilinear NW–SE sweeping abyssal hill and constructional volcanic features, from approximately Coral seamount to the EPR axis. Oscar is the seamount closest to the EPR axis. Associated constructional volcanic topography includes small-scale (<1 km diameter) cones, some with craters and linear arrays of cones on some of the seamount flanks, with the southern extents orientated sub-parallel to the ~350° abyssal hill trend. Other prominent volcanoes display calderas and breached calderas decorated with cones. Some of the seamounts have distinct morphological boundaries with respect to their neighbors, while others appear to have a component of coalesced volcanism that has resulted in more ridge-like features with dominant orientations that are either roughly N-S or E-W.

However, the limited (mostly single dredges with poor spatial constraints) and spatially disparate sampling of off-axis volcanic features has left the spatial distribution and scale of chemical heterogeneity in the near-ridge upper mantle unclear.

Here we present geochemical results of a multidisciplinary geochemical and geophysical investigation of the 8°20′N seamount chain, a line of individual and coalesced volcanic edifices that extend ~200 km west of the EPR near 8°20′N (Figure 1a). The spatial distribution of the volcanic cones, ridges, and mounds that comprise this seamount chain provides a unique opportunity to examine volcanic/tectonic interactions

in a fast-spreading MOR off-axis terrain proximal to a "leaky" transform (i.e., the Siqueiros Transform; Fornari et al., 1989). The orientation of the seamount chain perpendicular to the ridge yields spatial constraints important for determining the scale of mantle source heterogeneity, and melting systematics in a relatively well-studied MOR environment over a period that extends to ~2–3 Ma (Figure 1b). We systematically mapped the 8°20′N seamount chain using ship-based and autonomous underwater vehicle (AUV) *Sentry*-based multibeam, and used the human-occupied vehicle (HOV) *Alvin* to collect well-located, in-situ samples in addition to dredging. This study focuses on geochemical analyses of ~300 basaltic lavas collected from the 8°20′N seamount chain, and uses major and trace element abundances in conjunction with radiogenic isotope ratios to determine the petrogenesis of seamount lavas. Analytical results are used in petrologic models to investigate mantle components, melting systematics, and crustal magmatic processes required to account for the range of basalt compositions erupted along the seamount chain and within each seamount at small (<<1 km) spatial scales.

2. Geologic and Tectonic Setting of the 8°20′N Seamounts

The 8°20′N seamount chain is a ~200 km-long, east-west trending, linear array of volcanic constructs located on the western flanks of the East Pacific Rise (EPR) axis near 8°20′N. The eastern end of the chain is located ~20 km northwest of the western ridge-transform intersection (RTI) of the Siqueiros transform with the EPR (Figure 1a). The swath of volcanoes and coalesced volcanic ridges that comprise the chain are north of—and roughly parallel to—the western Siqueiros Fracture Zone (FZ) (Behn et al., 2002; S. Carbotte & Macdonald, 1992; Scheirer & Macdonald, 1995). The 8°20′N seamounts follow a relative motion trend of ~260°, while other seamount groups or chains (most notably the Lamont Seamounts to the north (Allan et al., 1989; Batiza et al., 1990; Fornari et al. 1988a, 1998b) are aligned along an absolute motion trend of ~330°.

On a regional scale, there are several important morphostructural features that dominate the fabric of the seafloor on the Pacific Plate between the Siqueiros and Clipperton transforms (Figure 1). The presence of intra-transform spreading centers in the Siqueiros transform (Fornari et al., 1989; Hebert & Montési, 2011; Perfit et al., 1996) and the evolution and reorganization of the plate boundary in this area (Pockalny et al., 1997) have resulted in several generally E–W trending structural lineaments on the Cocos Plate due east of the 8°20′N seamounts (Figure 1). These features are relicts of the northern Siqueiros transform deformation zone and have formed as the transform migrated southward over the past 1–2 Ma (P. M. Gregg et al., 2009; Pockalny et al., 1997). The seafloor fabric on either side of the EPR axis between Clipperton and Siqueiros (Figure 1) is predominantly comprised of abyssal hill structures that are primarily aligned along the ~350° trend of the EPR axis (Edwards et al., 1991; Goff et al., 1993). The exceptions to this are curved structures and pseudo-faults that demark the trajectory of the 9°03′N overlapping spreading center (Carbotte & Macdonald, 1992; V. D. Wanless et al., 2012).

Our recently acquired shipboard multibeam data also show the prominent association of EPR-parallel abyssal hill structures near the 8°20′N seamounts; however, south of the chain there are large swaths of curvilinear seafloor structures that bend southeastward into the western Siqueiros FZ (Figure 1). These curvilinear structures are present from the RTI to ~100 km from the EPR axis and abut the southern flanks of all the seamount volcanoes. South of the zone of curved seafloor fabric, there are packets of seafloor resembling lozenges of spreading center terrain formed within the transform that have been rafted westward and now occupy the northern margin of the Siqueiros FZ. These observations suggest dynamic, syn-tectonic volcanism has dominated crustal construction in the area south of the 8°20′N seamounts over the past several million years (Romano et al., 2017).

2.1. 2016 Research Expedition

A research expedition in November 2016 on RV *Atlantis* (AT37-05) sampled, mapped, and collected gravity and magnetic data across the 8°20′N seamount chain. Bathymetric data were collected using the shipboard EM122 multibeam system, magnetic data were collected using a surface-towed SeaSPY Overhauser Magnetometer System, and gravity data were measured using a BGM-3 sea gravimeter (geophysical results are reported by Romano et al., 2017). EM122 multibeam data gridded at 75-m resolution were collected over the

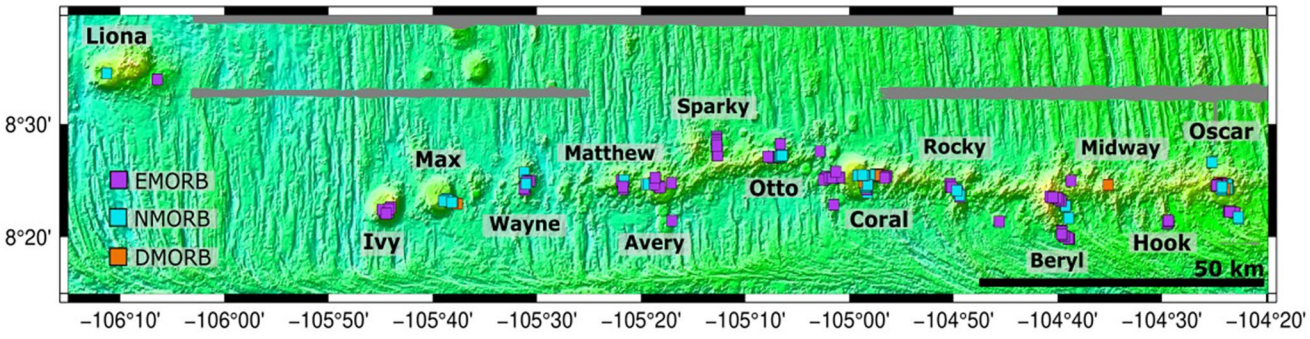

Figure 2. New EM122 bathymetry of the 8°20′N seamount chain with seamount names and sample locations (colored squares) recovered by *Alvin* and rock dredges where purple symbols are EMORB, NMORB are blue, and DMORB are orange.

entire study area (Figure 1b). AUV *Sentry* near-bottom high-resolution multibeam (~1-m grid resolution) data acquisition was focused on the summit and flank areas of several of the seamounts and provided the fine-scale morphological and structural information used to plan *Alvin* dives and select locations for in-situ sample collection. A total of 16 HOV *Alvin* dives and 19 rock dredges were conducted along the seamount chain, resulting in a collection of ~300 basaltic lava samples (Figure 2). A follow-up cruise, during which four additional *Alvin* dives along the 8°20′N seamount chain (AT42-06) were conducted, occurred in December 2018. Those data are not reported here.

2.2. Morphology of the Seamounts

The high-resolution mapping of the region allows insights into the range of morphologies of the seamount chain. The 8°20′N seamount chain is composed of a diverse array of volcanic constructs standing ~200–900 m in height above the surrounding seafloor. The eastern edge of the chain is comprised of east-west trending, nearly continuous ridges of coalesced volcanoes, with numerous smaller cones and mounds on the summits and flanks (Figure 1b). The volcanic construct in the chain closest to the EPR is ~22 km to the west of the axis (Oscar seamount). In addition to the coalesced ridges, there are deeper, EPR-parallel constructs that extend south-southeast from some of the seamount summits (e.g., Hook Ridge; Figure 2). The volcanoes in the chain that coalesced along E-W lineaments form constructional ridges, suggesting that the location and timing of volcanism have been episodic in terms of erupted volume relative to spreading rate (Figure 1). The coalesced ridges do not persist beyond ~125 km west of the EPR. Instead, the chain transitions to larger, more rounded, individual volcanoes with craters (Figure 1). The westernmost seamount examined is Liona (~209 km west of axis), one of the largest in the chain, but is offset significantly to the north.

Morphological and observational evidence suggest relatively recent volcanism persists along the chain, even on edifices near the middle of the chain, nearly 100 km from the EPR axis. The intact pillow flows are relatively fresh, with only thin Mn-coatings and limited sediment cover (Fabbrizzi et al., 2020). The seamounts do not appear to systematically age with distance from the EPR, since evidence for recent volcanism persists across much of the seamount chain. Additionally, rift zone-like extensions of constructional volcanism that trend S-SE from the main edifices in the eastern half of the chain (Figure 1b) suggest longer term magmatic supply during which the central volcanoes grew and some developed the elongated (N-S) shapes that were influenced by the stress field created by spreading dynamics as the seafloor was deformed along the northern margin of the Siqueiros FZ.

3. Methods

3.1. Major Elements

Basaltic glass, chipped from the outer rind of each lava, was used for geochemical analyses. When present, clean, phenocryst and alteration-free basaltic glass was selected. Three to five glass chips were handpicked from each sample using a binocular microscope and were mounted in 1-inch epoxy disks for geochemical analysis. The mounts were polished in 6, 3, and 1 μm diamond grits, and then hand-polished using 1 μm alumina grit.

Major element concentrations of the 281 lavas that contained glass were determined using the CAMECA SXFive-FE microprobe at the University of Florida and a JEOL 8800 electron microprobe at USGS in Denver. The accelerating voltage in both labs was 15 kV, beam current was 20 nA, and beam diameter was 10 μm. Count times varied for different elements. At the University of Florida and USGS, Na was analyzed first for 10 s because of its volatile nature during analysis. Mg, Si, Al, Fe, Mn, and Ca were also analyzed for 10 s each on all 281 samples. Ti, P, K, and Cl were analyzed for 20 s. Ni, Cr, and S were measured for 10 s during some of the initial sample analyses but were often below detection limits and thus unmeasured on subsequent samples. 10 spots were measured on each glass and averaged. Secondary basalt standard ALV-2392 (Perfit et al., 2012) was run for approximately every 10–15 samples to account for any instrument drift. The measured standard values are provided in Supplement 1. A set of 52 samples was analyzed at both the labs for interlab comparison, which—based on measured standards JDF-D2 and ALV-2392 (at the University of Florida), and A99 and USNM (at USGS)—resulted in relative percentage corrections of −7% for Na_2O and −3% for CaO measurements from USGS. The remaining major element concentrations in the glass standards in each lab measured within one standard deviation and required no adjustment. Duplicate analyses are presented in Supplement 2. With the exception of Na_2O (RSD % = 6.3), precision for all other major elements was below 4 RSD%. Major element concentrations and uncertainties for analyzed basalt glasses are reported in Table S1.

3.2. Trace Elements

Using the same glass chips analyzed by microprobe, trace element concentrations were determined on 148 samples using a Laser Ablation (UP213 Nd-YAG New Wave Research laser) ThermoElectron X-Series II Quadrupole Inductively Coupled Plasma Mass Spectrometer (LA-ICP-MS) at Boise State University. The instrument was calibrated using USGS and NIST610 glasses. The repeat rate was 10 Hz and dwell time 30 s using ∼0.278 mJ of energy. Each glass sample was ablated five times (three on one chip and two on another where multiple chips were available for a given sample) using 80–110 μm rounded spots and averaged. Glass standards used included KL2, ML3B, StHls, T1, ATHO, BHVO, BCR, and BIR, with BHVO, BCR, and BIR analyzed at every five samples. Precision was generally below 6 RSD% with a few exceptions: Tm, Lu, Ta, Pb, Th, and U measured between 6 and 9 RSD%. Glass trace element contents are reported in Table S2 and measured standard values are reported in Supplement 3.

3.3. Radiogenic Isotopes

Radiogenic isotopes were collected on 19 geochemically and spatially diverse basalts at the University of Florida. Approximately 50 mg of fresh, phenocryst-free glass was handpicked using a binocular microscope. To avoid any remaining alteration and manganese coating on these samples, the glass chips were cleaned using a combination of leaching methods (Goss et al., 2010; Sims et al., 2002; C. L. Waters et al., 2011). Glass chips were sonicated in DI water for 20 min and rinsed. The glasses were placed in capped Teflon and leached in 35% H_2O_2 for 15 min on a hot plate at 130°C. The samples were rinsed thrice in DI, then in capped Teflon leached in 2 mL of 6 M HCL for either 30 or 60 min (depending on the amount of remaining manganese coating) at 130°C. The samples were rinsed in DI and then sonicated for 15 min in DI before rinsing thrice in DI water. The samples were then dried overnight in an oven at 50°C. Clean glasses were digested in 3 mL HNO_3 + 1.5 mL HF, and after evaporated drying, dissolved in 6 N HCl and subsequently evaporate dried. The dried residue was dissolved and separated for Pb, Sr, and Nd using column chemistry, following the methods described in Goss et al. (2010): Pb was separated through 100 μL Teflon columns in HBr eluent, then washed 3x in 1 mL 1 N HBr, and collected in 1 mL 3N HNO_3. Sr and Nd were collected subsequently using 1 N HBr and purified for analysis. Biorad AG50W resin columns were used to separate Sr from REE and Nd was separated from REE through columns of 2 mL of Ln-Resin. Pb, Sr, and Nd isotopes were then measured at the University of Florida using a Nu-Plasma HR multicollector (MC) ICP-MS, using the methods described in Kamenov et al. (2008) and Goss et al. (2010). Standards NBS-981, NBS-987, and JNdi-1 were run every 5–6 samples for Pb, Sr, and Nd, respectively, and the averages are reported in Supplement 4. Sr, Nd, and Pb isotopic ratios and uncertainty (2 sd) for the samples and several duplicate analyses from the same sample aliquot are reported in Table S3.

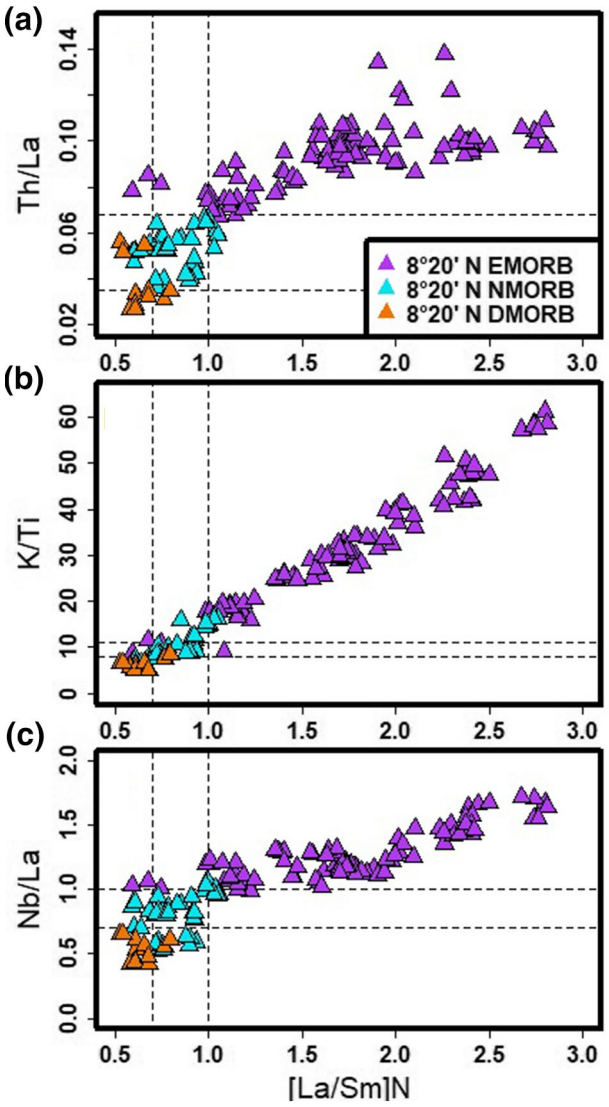

Figure 3. Incompatible element ratio variations and basalt classification scheme of the 8°20′N seamount lavas using $[La/Sm]_N$, Th/La, K/Ti, and Nb/La ratios relative to existing classification systems (Arevalo & McDonough, 2010; Perfit et al, 1994; Shimizu et al., 2016; Sinton et al., 1991; M. C. Smith et al., 2001). Dashed lines represent approximate boundaries for EMORB, NMORB, and DMORB compositions used for this study based on these classification systems. Some samples do not perfectly fall within each category every time, so in those cases, all of these systems are combined to decide into which category they belong.

4. Geochemical Results

Samples collected from the 8°20′N seamounts are extremely heterogeneous on small scales. Each basalt is classified as a DMORB, NMORB, or EMORB (Figure 3), primarily based on their Th/La ratio (Shimizu et al., 2016) in conjunction with $(La/Sm)_N$ and K/Ti ($100*[K_2O/TiO_2]$) ratios (Arevalo & McDonough, 2010; Perfit et al., 1994; Sinton et al., 1991; M. C. Smith et al., 2001). Because the lavas form a near-continuum rather than distinct geochemical groups (Figures 3–5), these parameters are used collectively to classify each lava. DMORB from the seamounts typically have Th/La, $(La/Sm)_N$, and K/Ti ratios less than 0.035, 0.60, and 8, respectively, whereas EMORB ratios are commonly greater than 0.068 (Th/La), 1.0 ($[La/Sm]_N$), and 16 (K/Ti), and NMORB fall between these values (Figure 3). Based on this classification scheme, we analyzed 176 EMORB, 86 NMORB, and 19 DMORB lavas.

Individual seamounts have erupted multiple MORB-types (e.g., Oscar or Coral; Figures 2 and 4), and in some cases DMORB and EMORB outcrops are located <1 km from each other. For example, on top of the Oscar seamount (located ~22 km from the axis), DMORB were recovered within ~600 m of the most enriched EMORB lava flow. Lava compositions across the entire chain form a continuum from mafic basalts (up to 10.25 wt% MgO) to evolved basalts (<5 wt.% MgO; Figure 4). Some lavas are highly incompatible element depleted and enriched compared to some of the most enriched and depleted basalts recovered from non-hotspot-related seamounts in the north eastern Pacific. The rather limited range of SiO_2 contents (~47–51 wt%) in all of the samples (Figure 6) is notable considering the large range of total alkalis ($Na_2O + K_2O$ = 2.4–6.1 wt%). EMORB on average have lower MgO contents (~7.4 wt%) than the NMORB (~8.6 wt%) and DMORB (~9.1), suggesting that the EMORB are typically more evolved. Total alkalis exhibit a strong linear correlation with K/Ti (r = 0.84). Only the most enriched samples (K/Ti > 45) are slightly Ne-normative (<3 wt%).

4.1. EMORB

Based on incompatible element ratios, the majority (63%) of the seamount lavas collected are EMORB (Figure 5), which is a high percentage compared to the adjacent 8°–10°N EPR ridge axis segment (<5%). Relative to NMORB, EMORB are characterized by higher K/Ti ratios (17–61), relatively low CaO/Al_2O_3 ratios (mostly between 0.50 and 0.75), especially for the samples with less than 8 wt% MgO, and generally lower MgO contents (although they range from 4.61 to 9.01 wt%; Figure 4). Mg# varies from 44 to 64 (see Supplement 5). At similar MgO contents (or Mg#), EMORB Na_2O contents are elevated relative to D- and NMORB (2.40–4.29 wt%), whereas EMORB FeO (8.08–12.0 wt%) and CaO (10.8–11.78 wt%) concentrations are relatively low compared to NMORB and DMORB. The ratios of light to middle rare earth elements (LREEs and MREEs) in EMORB lavas are high (i.e., $[La/Sm]_N$ ranges from 1.0 to 2.8, with the exception of three samples with $[La/Sm]_N$ ratios as low as 0.74 but high Th/La), as are MREE to heavy (HREE) ratios (i.e., $[Gd/Yb]_N$ ~ 1.1–2.2; see S6). The ratios of highly incompatible elements with similar distribution coefficients (i.e., Nb/La ~ 0.97–1.7) are also higher than in NMORB and DMORB lavas. Additionally, the EMORB have more radiogenic $^{87}Sr/^{86}Sr$ (0.702693–0.703198; Figure 7) and Pb isotopes (i.e., $^{206}Pb/^{204}Pb$ 18.536–18.714, and less radiogenic $^{143}Nd/^{144}Nd$ (0.512959–0.513104) than both DMORB and NMORB (Figure 7).

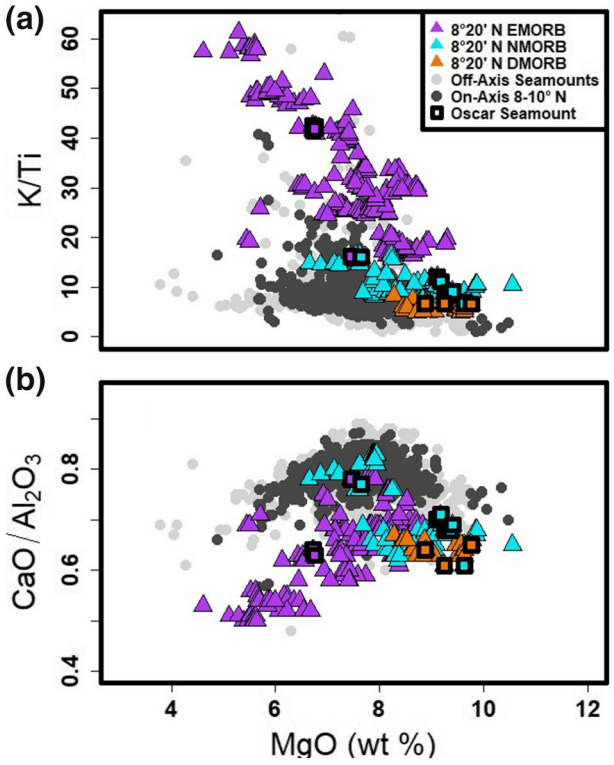

Figure 4. (a) MgO (wt%) versus K/Ti ($100*K_2O/TiO_2$) of the 8°20′N seamount lavas color-coded by MORB type (EMORB purple; NMORB blue; DMORB orange) as discussed in the text. On-axis 8°–10°N samples (solid black circles) are glass analyses of basalts collected directly from the EPR ridge axis between the Siqueiros and Clipperton transform faults. Off-Axis Seamounts dataset (light gray circles) includes glasses from seamount lavas within ~200 km of the ridge from ~5°–15°N (all references for samples available in Supplement 7). Oscar seamount samples (bold squares) are highlighted to show the variability on a single seamount ~22 km from the EPR ridge axis. Note the near-continuum of data from most depleted K/Ti (DMORB) to most enriched K/Ti (EMORB). (b) MgO (wt%) versus CaO/Al_2O_3 of the 8°20′N seamount lavas compared with both on-axis EPR and off-axis seamount datasets (as above). The 8°20′N seamounts have distinctly lower CaO/Al_2O_3 ratios and crystallization trends that differ from typical EPR MORB .

4.2. NMORB

The second most abundant lava composition observed is NMORB (30%). These lavas are similar to NMORB lavas observed on-axis at the EPR (Figures 4, 6 and 7), but extend to more mafic compositions (Figure 4). Seamount NMORB are characterized by moderate K/Ti ratios (6.7–16), moderate to high MgO contents (6.65–10.6 wt%) and Mg# (53–68), and elevated CaO/Al_2O_3 ratios (0.60–0.85). NMORB Na_2O contents are lower than EMORB but are comparable to DMORB (2.44–3.27 wt%) at the given MgO contents. Ratios of LREEs to MREEs (i.e., $[La/Sm]_N \sim 0.59–1.0$), and MREEs to HREEs (i.e., $[Gd/Yb]_N \sim 0.99–1.4$) are lower than those of EMORB, but closely resemble DMORB (Figure 5). FeO contents span the same range as EMORB and DMORB (8.40–12.3 wt%). Ratios of highly incompatible trace elements with similar distribution coefficients (i.e., Nb/La ~ 0.52–1.1) are lower than EMORB and generally higher than most DMORB. The NMORB also have more radiogenic $^{87}Sr/^{86}Sr$ (0.702630–0.702743) and Pb isotopic ratios (i.e., $^{206}Pb/^{204}Pb$ are 18.173–18.781) than DMORB and have $^{143}Nd/^{144}Nd$ ratios (0.513043–0.513119) more radiogenic than EMORB but less radiogenic than DMORB.

4.3. DMORB

The least abundant lava composition sampled on the seamounts is DMORB (7%), which are characterized by a strong depletion of the most highly incompatible elements (Figures 4 and 5). They are generally more mafic lavas than the EMORB and NMORB (with a narrow range of MgO contents from 8.03 to 9.35 wt%; Mg# 58–67). The DMORB also have the lowest K/Ti ratios (<8.5) (Figure 4). Similar to NMORB, DMORB have a small range of silica contents (<49 wt%), CaO/Al_2O_3 ratios (0.60–0.70), and FeO contents compared with EMORB (7.80–10.6 wt%). DMORB Na_2O contents are lower than EMORB, but are comparable with NMORB (2.34–3.29 wt%) at comparable MgO contents. DMORB LREE to MREE ratios are lower than NMORB (i.e., $[La/Sm]_N$ 0.53–0.80), but the MREE to HREE ratios are greater (i.e., $[Gd/Yb]_N \sim 0.86–1.5$) and overlap the more elevated EMORB heavy rare earth elements (Figure 5). As expected, DMORB highly incompatible element ratios are the lowest among all the samples (e.g., Nb/La ~ 0.42–0.65). The DMORB consistently have less radiogenic $^{87}Sr/^{86}Sr$ (0.702333–0.702607) and Pb isotopes (i.e., $^{206}Pb/^{204}Pb$ 17.911–18.536) than EMORB and NMORB, and more radiogenic $^{143}Nd/^{144}Nd$ isotopes (0.513058–0.513211) (Figure 7). DMORB even have notably less radiogenic $^{87}Sr/^{86}Sr$ and Pb isotopes (and more radiogenic $^{143}Nd/^{144}Nd$ isotopes) than EPR MOR samples from the nearby axial region (Figure 7).

4.4. Geochemical Trends

Geochemical comparisons and trends are useful for distinguishing parental magmas and subsequent petrologic processes that may be responsible for generating the heterogeneity observed in seamount lavas. The large range in K/Ti (and other incompatible trace element ratios) together with variations in radiogenic isotopes substantiate the existence of multiple parental basaltic magmas. The fact that there are very few high K/Ti EMORB with mafic major element characteristics makes it difficult to determine early crystallization histories and liquid lines of descent (LLD). For example, EMORB that have a range of ~20–60 K/Ti (Figure 4) contain subgroups with similar K/Ti ratios that have different major element trends as a function of decreasing MgO contents. In general, with decreasing MgO, Al_2O_3 contents in DMORB and NMORB decrease, but EMORB Al_2O_3 contents remain relatively constant or increase only slightly, suggesting suppression of plagioclase crystallization (Figure 6). Based on these observations as well as preliminary fractional

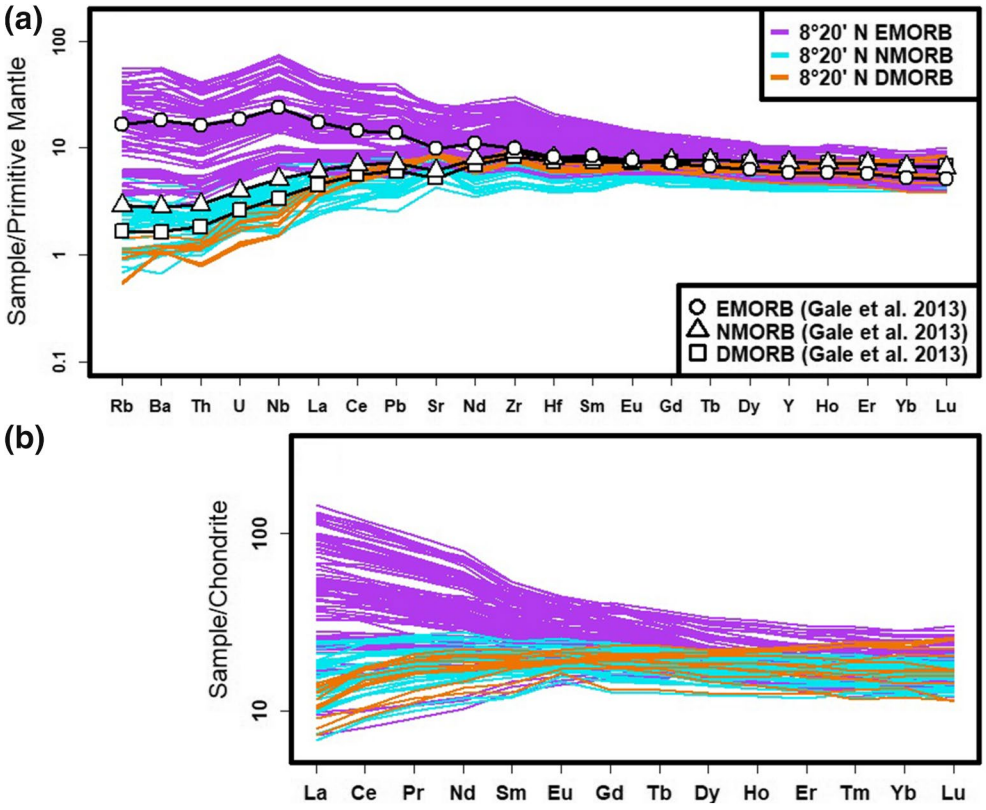

Figure 5. (a) Primitive mantle-normalized (Sun & McDonough, 1989) trace element diagram of the 8°20′N seamount lavas colored according to MORB type (EMORB purple; NMORB blue; DMORB orange) as described in the text. Average EMORB, NMORB, and DMORB concentrations from Gale et al. (2013) are shown for comparison. Note the relative slopes of the most incompatible trace elements (from Rb to Nd) for each MORB-type. DMORB are characteristically more depleted in the most highly incompatible trace elements than NMORB (slight depletion) and EMORB, while EMORB show variable degrees of enrichment—up to ~50 times that of DMORB. The less incompatible elements show significantly less enrichment relative to DMORB and no overall heavy REE depletion. (b) Chondrite-normalized (McDonough & Sun, 1995) rare Earth element (REE) diagram of the 8˚20′N seamount lavas colored by MORB type as described above.

crystallization modeling (Conrad et al., 2018), different LLD are necessary to characterize each MORB-type (and subtype) differentiation trends, due to different conditions of crystallization (e.g., T, P, fO_2, H_2O) prior to eruption.

5. Discussion

5.1. Comparison of 8°20′N Seamount Chain Basalts to Regional EPR Lavas

Studies of near-EPR seamount lavas have shown that the diversity of their compositions may indicate tapping of melts that ascend vertically from the outer regions of the melting triangle, thus bypassing the axial magma chamber and preserving a wider compositional range than is observed on-axis (Allan & Batiza, 1987; Batiza & Niu, 1992; Batiza et al., 1989, 1990; Brandl et al., 2012; Niu & Batiza, 1997a, 1997b; Niu et al., 2002; Perfit & Chadwick, ; Shimizu et al., 2016; Zindler et al., 1984). Basalts erupted along the 8°20′N seamount chain are chemically more heterogeneous and enriched in incompatible element ratios than lavas erupted on-axis along the adjacent EPR segment (Figures 4, 6, and 7; References available in Supplement 7). For example, EPR MORB erupted on-axis (within 4 km) between 8° and 10°N (hereafter referred to as "on-axis 8–10°N″) have relatively limited major and trace element compositions (1–40 K/Ti, 0.31–2.3 $[La/Sm]_N$) compared to the seamount lavas (5–61 K/Ti and 0.53–2.8 $[La/Sm]_N$) (Figure 4; S6). Average K/Ti and $[La/Sm]_N$ ratios are far lower for on-axis 8°–10°N samples (~8 K/Ti and 0.72 $[La/Sm]_N$) than the 8°20′N seamounts (~24 K/Ti and 1.39 $[La/Sm]_N$). These results support previous studies that suggest the nearly

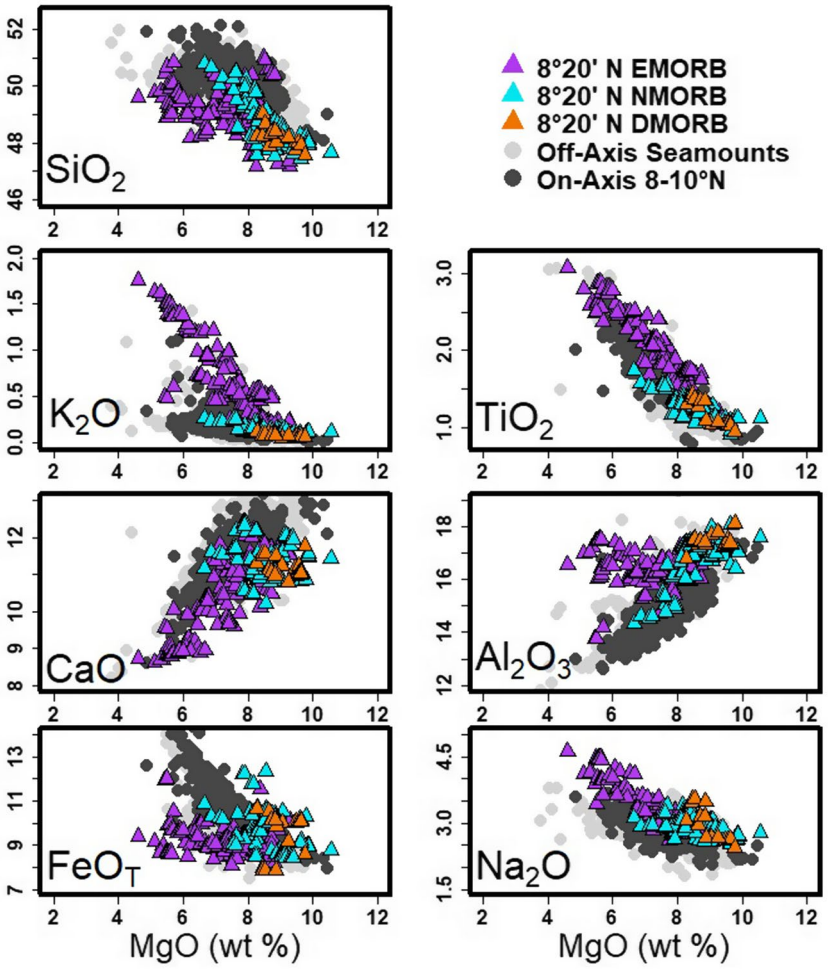

Figure 6. Major element bivariate diagrams of the 8°20′N seamount lavas colored by MORB-type. Local on-axis 8°–10°N samples (black circles), and data from other near-EPR, off-axis seamounts not from this study (light gray circles) are shown for comparison. 8°20′N seamount EMORB lavas have notably lower FeO(total) and CaO but higher Al_2O_3 and K_2O than DMORB and NMORB, including those from the EPR at given MgO contents. See Supplement 5 for similar plots versus Mg#.

ubiquitous melt lenses on-axis are relatively efficient at homogenizing melts prior to eruption (Perfit & Chadwick, ; Rubin et al., 2009; Sinton & Detrick, 1992) and highlight the role the axial magmatic system plays in obscuring important chemical characteristics of the sub-oceanic mantle.

The 8°20′N seamount basalts span the entire range of major element, trace element, and radiogenic isotope ratios of other northern EPR off-axis seamount lavas (Figures 4, 6, and 7; References available in Supplement 7), hereafter referred to as "off-axis seamounts." In some cases, the 8°20′N seamount basalts even extend beyond the range of off-axis seamount lavas. Isotopically, the 8°20′N seamount lavas have a similar range as on-axis (and off-axis) EPR MOR lavas (Figure 7), suggesting that they share common isotopic sources. However, the high spatial resolution of sampling (<1 km scales) and the orientation of the 8°20′N seamounts relative to the EPR allows the off-axis chemical variability to be examined in much greater detail. Thus, we evaluate the influence of the variations in extents of melting and mantle heterogeneity over short length scales and with distance from the EPR axis.

5.2. Compositional Variability with Distance from the Ridge Axis

Numerical and geochemical studies suggest that there may be a maximum distance (~20–40 km) over which mantle melts can be efficiently focused and transported to the ridge axis (Figure 9; Behn & Grove, 2015;

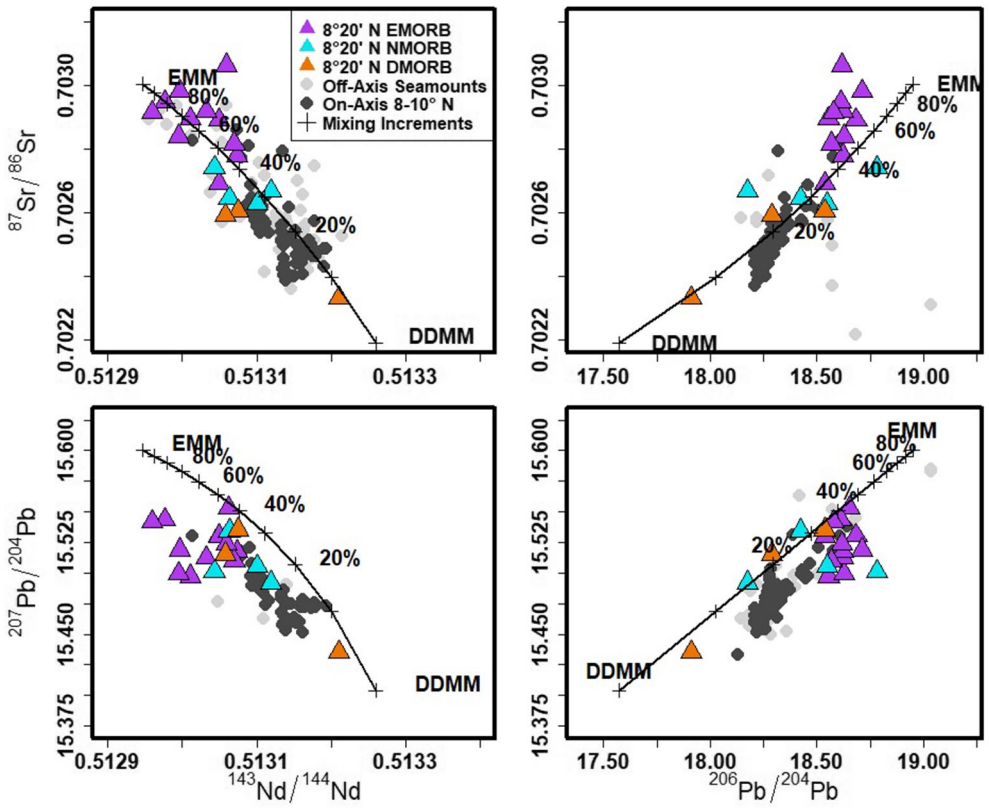

Figure 7. Radiogenic isotope (Pb, Sr, and Nd) ratios of the 8°20′N seamount lavas (triangles) colored by MORB type compared with on-axis 8°–10°N samples (black circles) and off-axis seamounts (light gray circles). Mid-ocean ridge mantle reservoirs EMM (Enriched MORB Mantle from Donnelly et al., 2004) and DDMM (depleted MORB Mantle from Workman & Hart, 2005) are shown as mantle end-members for the seamount compositions. Binary source mixing models (black line) between EMM and DDMM sources are shown with black plus signs, indicating 10% increments.

A. J. Turner et al., 2017; V. D. Wanless et al., 2014). Consequently, melts from the outer edges of the melting region may be excluded from on-axis eruptions and instead re-fertilize the overlying depleted mantle (le Roux et al., 2006; Plank & Langmuir, 1992), and/or become a source for off-axis volcanism (Figure 9; Perfit et al., 1994). Variable extents of melting of a chemically homogeneous mantle source will result in variable ratios of trace elements with different incompatibilities during melting (Bo et al., 2018; O'Hara, 1985). Thus, magmas produced by greater extents of melting directly beneath the ridge axis are expected to have distinctly lower incompatible trace element concentrations and lower ratios of incompatible to less incompatible trace elements compared to magmas produced by lower extents of melting away from the ridge axis. These observations combined with the shape of the melting regime suggest that there should be systematic changes in melt compositions produced in the melting region with distance from the ridge axis, assuming the source mantle is homogeneous, the seamounts are tapping melts produced in the mantle directly below, and that the seamounts have not migrated significantly since emplacement of the lavas sampled.

There is no systematic variation in lava chemistry with distance from the ridge axis along the ~200 km seamount chain (Figure 8). Instead, EMORB, NMORB, and DMORB lavas are observed along the entire length of the chain, including the seamounts nearest the ridge axis (Figures 1 and 8). In fact, some individual seamounts are comprised of lavas ranging in composition from DMORB to EMORB over relatively small (<1 km) spatial scales (e.g., Oscar, only 22 km from the ridge axis). Thus, the seamounts are not synchronously tapping melts produced in various parts of the melting triangle in a homogeneous mantle.

Alternatively, it is possible that individual seamounts are built over time from repeated eruptions as the Pacific plate migrates away from the ridge axis across the length of the melting triangle, and thus sequentially tapping different portions of the melting triangle over time (E. E. Davis & Karsten, 1986). In this case, the

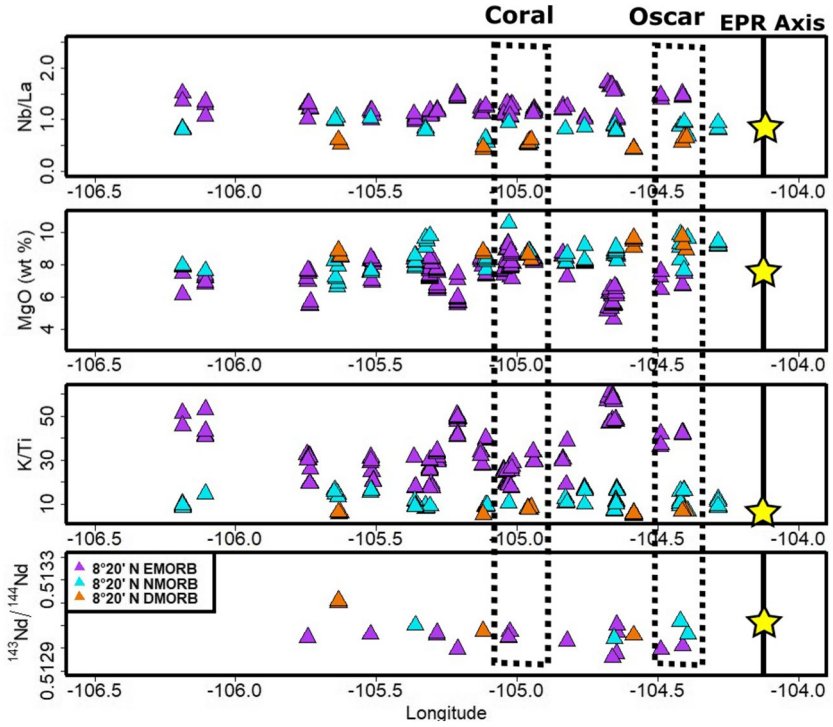

Figure 8. Spatial variation in 8°20′N seamount lava chemistry (Nb/La ratios), MgO (wt%), K/Ti ratios, and $^{143}Nd/^{144}Nd$ ratios with distance from the ridge axis (longitude right to left) with seamount samples colored by MORB type. Vertical black lines represent the location of the East Pacific Rise axis, and the yellow stars represent the average composition on-axis for each element concentration or ratio. Dotted rectangles outline the two seamounts discussed in the text (Oscar and Coral) to demonstrate extreme variability on single-seamount scales. There is no systematic variation in the degree of incompatible element enrichment, major element concentrations or ratios, or radiogenic isotopes with distance from the ridge axis. All lava types are found across nearly the entire length of the seamount chain. Seamount NMORB compare best with the on-axis average for every element concentration/ratio.

composition of lavas erupted on each seamount should transition from more depleted at the base to more enriched at the top with time (assuming central vent eruptions). However, the detailed sampling up the slope of numerous volcanic constructs shows no systematic change in lava composition with recovery depth on any of the seamounts (Supplement 8). It is possible that systematic changes are buried by later eruptions or were not sampled; however, both D and EMORB lavas were sampled on the top of the same seamount (Oscar), nearest to the ridge axis (Figure 8). This suggests that a range of lava compositions can be erupted at a single seamount over relatively short timescales and relatively close to the ridge axis. Thus, the observed spatial distribution of lava compositions suggests that the seamount chain was not produced simply by passively tapping magmas produced in the underlying the MOR melting triangle (Figure 9).

5.3. Mantle Source Variability in Seamount Lavas

Radiogenic isotope ratios, unlike major element concentrations and trace element ratios, are unchanged by mantle melting and crystallization, and thus reflect mantle source compositions (McKenzie et al., 2004; Niu et al., 1996; Stracke & Bourdon, 2009; Zindler et al., 1984). Globally, radiogenic isotope studies suggest that the MOR mantle source is predominantly comprised of a depleted component; however, numerous studies of basaltic MOR lavas suggest that there are additional components feeding the global MOR ridge system (Batiza & Niu, 1992; Donnelly et al., 2004; Mallick et al., 2019; Perfit et al., 1994; Shimizu et al., 2016; C. L. Waters et al., 2011; R. K. Workman et al., 2004). Studies that have examined the petrogenesis of EMORB lavas erupted on or near the 8°–10° EPR ridge axis invoke melting of a small volume of an enriched component, in addition to a depleted component, to account for the range of radiogenic isotope ratios observed (Perfit et al., 2012; Shimizu et al., 2016; M. C. Smith et al., 2001; C. L. Waters et al., 2011). These studies

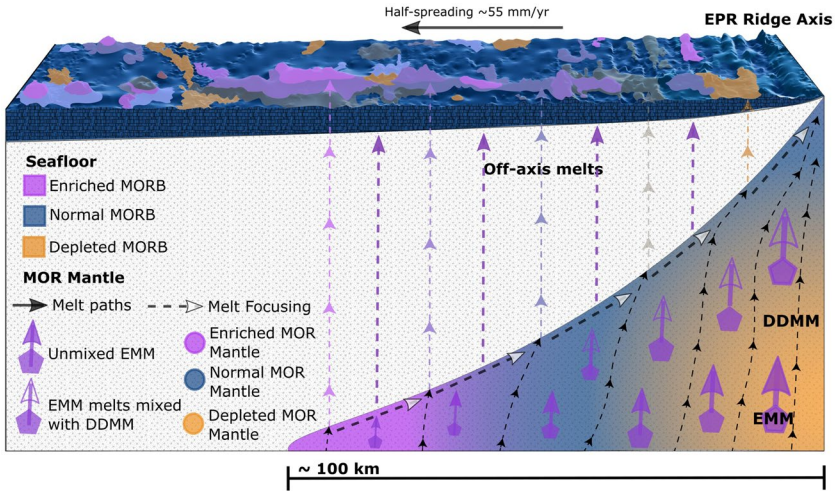

Figure 9. Conceptual model for melting a heterogeneous mantle, evaluated using data from the 8°20′ N seamount chain basalt compositions. The EPR axis and half-spreading direction are shown at the top. Colors of the seafloor bathymetry of the chain of seamounts on the surface reflect compositions found along the seamounts (EMORB, NMORB, and DMORB). The triangle on the lower right side beneath the ridge and seamounts represents the region of mantle melting on a single side of the ridge. The DDMM component is represented by the continuum of purple, blue, and orange background colors which reflect the compositions of mantle melts based on degrees of melting as a function of the height of the triangle (i.e., the distance melts travel and therefore the extent of melting they undergo). In this diagram, the purple background represents the lowest degrees of melting (resulting in incompatible element enriched melts), blue represents intermediate degrees of melting, and orange represents the highest degrees of melting (resulting in incompatible element depleted melts). The EMM component is superimposed as purple pentagons whose melts are the purple arrows. The filled arrows represent initial melts of EMM that have not yet mixed with DDMM. The open arrows represent EMM melts that have likely mixed with DDMM, obscuring their enriched signature (i.e., directly beneath the axis these signatures are lost to mixing and high degrees of melting). Theoretical melt paths are shown as arrows with dashed lines, indicating that some melts rise through the melt triangle, reach the top of the melt region and focus toward the ridge (within ~20 km of the ridge), while others ascend vertically to the surface (by-passing on-axis mixing).

combined with investigations of ultramafic rocks in ophiolites (e.g., Boudier & Coleman, 1981) and dredges from fracture zones have led to the hypothesis that enriched signatures result from melting of pyroxenite veins that are embedded in the upper mantle (Gill et al., 2016; Gleeson et al., 2020; Hirschmann & Stolper, 1996; Mallick et al., 2015; Niu et al., 1999; Stracke et al., 1999; C. L. Waters et al., 2011; Yang et al., 2020). However, the composition and physical distribution of this petrochemical component within the near-ridge mantle has not been well constrained, primarily because the signatures are often obscured on-axis.

Lavas erupted along the 8°20′N seamount chain have a wide range of radiogenic isotope ratios compared to the majority of lavas erupted on-axis (Figure 7), providing evidence for a heterogeneous mantle near the northern EPR. Although other seamounts in the region also have variable isotope ratios, the 8°20′N lavas span the entire range of lavas collected at all northern EPR off-axis seamounts combined (Figure 7). To determine the source and extent of mantle heterogeneity, we compare seamount lava compositions to two commonly used end-member MOR mantle components (Figure 7); Enriched MOR Mantle (EMM) from Donnelly et al. (2004) and Depleted MOR Mantle (DDMM) from Workman & Hart (2005).

The DDMM component is representative of the most depleted end-member of the depleted upper mantle (Workman & Hart, 2005). The commonly used average DMM (Workman & Hart, 2005) cannot account for the most depleted (DMORB) lavas erupted along the seamount chain, suggesting that the regional mantle is composed of a more depleted end-member (DDMM). By contrast, the EMM component is believed to be representative of a reservoir composed of enriched material (more radiogenic Sr and Pb, less radiogenic Nd) that is unrelated to a mantle plume (Donnelly et al., 2004). The addition of an enriched component in the upper mantle without the presence of a nearby plume has been attributed to subducted and recycled oceanic crust, lithosphere, and/or sediments, which through time are metasomatizing and/or mixing into the depleted upper mantle (e.g. Niu & Batiza, 1997b; Niu et al., 2002; Shimizu et al., 2016; Yang et al., 2020).

This results in a volumetrically small, but perhaps ubiquitous EMM component distributed throughout the upper mantle (Sobolev et al., 2007; Stracke & Bourdon, 2009).

While some studies of mantle heterogeneity invoke a pyroxenite source to explain incompatible element enrichment (Gill et al., 2016; Hirschmann & Stolper, 1996; Mallick et al., 2015; Niu et al., 1999; Stracke et al., 1999; C. L. Waters et al., 2011; Yang et al., 2020; G. L. Zhang et al., 2012), only lherzolitic source compositions are used here to model the geochemical variability. If any significant amount of garnet-bearing pyroxenite or eclogite was partially melted in the source lithology, a heavy rare earth element (HREE) depletion should be observed in erupted lavas. However, the $(Gd/Yb)_N$ ratios in the 8°20′N lavas change very little in even the most enriched EMORB, indicating a lack of HREE depletion that would characterize a garnet bearing source (Figure 5b; Supplement 6). Thus, a garnet signature from pyroxenite partial melting (Hirschmann & Stolper, 1996) is not required. Similarly, metasomatism is also commonly invoked to explain major and trace element heterogeneity in ocean island and MOR settings (Niu et al., 2002, 2012; Pilet et al., 2008, 2011). Low-degree melt metasomatism at the base of oceanic lithosphere can explain enrichment of fluid-mobile incompatible elements; however, radiogenic isotopes require ancient origins (Niu et al., 2002), potentially involving a subducted lithosphere component not clearly identifiable by radiogenic isotopes in this study. Melting/mixing models using combinations of DDMM and EMM can, on a first order, adequately explain the range of compositions, removing the need to include a pyroxenitic lithology or metasomatic fluid interactions. To determine the mantle sources contributing to the range of compositions observed along the 8°20′N seamount chain, we compare the isotopic ratios of the mantle end-members with those of the seamount lavas (Figure 7). Several EMORB lavas have radiogenic isotope ratios similar to the EMM end-member, while DMORB lavas are closer to the DDMM end-member (Figure 7). All other seamounts have lava compositions that generally lie between these two end-member components. Binary mixing models suggest that melting of a mantle composed of various mixtures of these two components (or mixing of the primary melts from these sources) can account for a wide range of the isotopic signatures. However, several lavas lie off this binary mixing curve, suggesting that a third enriched component may be present. Regardless, multiple mantle sources are required to explain the radiogenic isotope ratios of seamount lavas.

5.4. Constraining the Impacts of Source Versus Melting

Co-variation of incompatible trace element ratios with radiogenic isotope ratios can be used to evaluate the effects of melting versus source composition (Figure 10). To differentiate and constrain the impacts of melting versus source variability in the generation of off-axis lavas, trace element ratios ($[La/Sm]_N$ and Nb/La) are used in forward melting models (Figure 11). $(La/Sm)_N$ ratios are sensitive to variations in extent of mantle melting due to their distinct partition coefficients during melting (higher ratios indicate lower extents of melting). However, this is not a perfect assumption since enrichments in the mantle may preferentially melt and contribute to a greater extent to resulting melt-induced mixtures (Niu & Hekinian, 2004). By contrast, Nb and La have similar partition coefficients during melting, but can vary with source; thus, variations in Nb/La ratios can be used as a proxy for heterogeneity in the mantle in the absence of radiogenic isotope analyses (Hofmann, 1997). If source variability is the only process controlling the composition of 8°20′N lavas, then trace element ratios should systematically vary with radiogenic isotope ratios (Figure 10). While this is observed in some isotope-trace element ratio pairs (Nd isotopes and $[La/Sm]_N$ of EMORB and NMORB), it is inconsistent across all trace element and radiogenic isotope ratios (Pb isotope ratios do not consistently correlate with trace elements $[La/Sm]_N$; Figure 10) unless they share common incompatibilities (Nb/La correlates well with Nd isotope ratios; Figure 10). Interestingly, EMORB lavas have relatively limited Pb isotope ratios, but vary in $(La/Sm)_N$ ratios. By contrast, NMORB and DMORB vary in Pb isotope ratios and have limited in $(La/Sm)_N$ ratios. This suggests that source variability and melting processes beneath the 8°20′N seamount chain may influence MORB-types differently.

To model melting of a heterogeneous lherzolitic mantle source, we first determined the starting compositions of the end-member mantle components and then calculated melt compositions of various mixtures of those components using alphaMELTS (Figure 11). The trace element contents in mantle end-members may be variable and are difficult to constrain using erupted lavas because they are highly influenced by both the source mineralogy and melting process. To estimate trace element contents in both lherzolite end-members

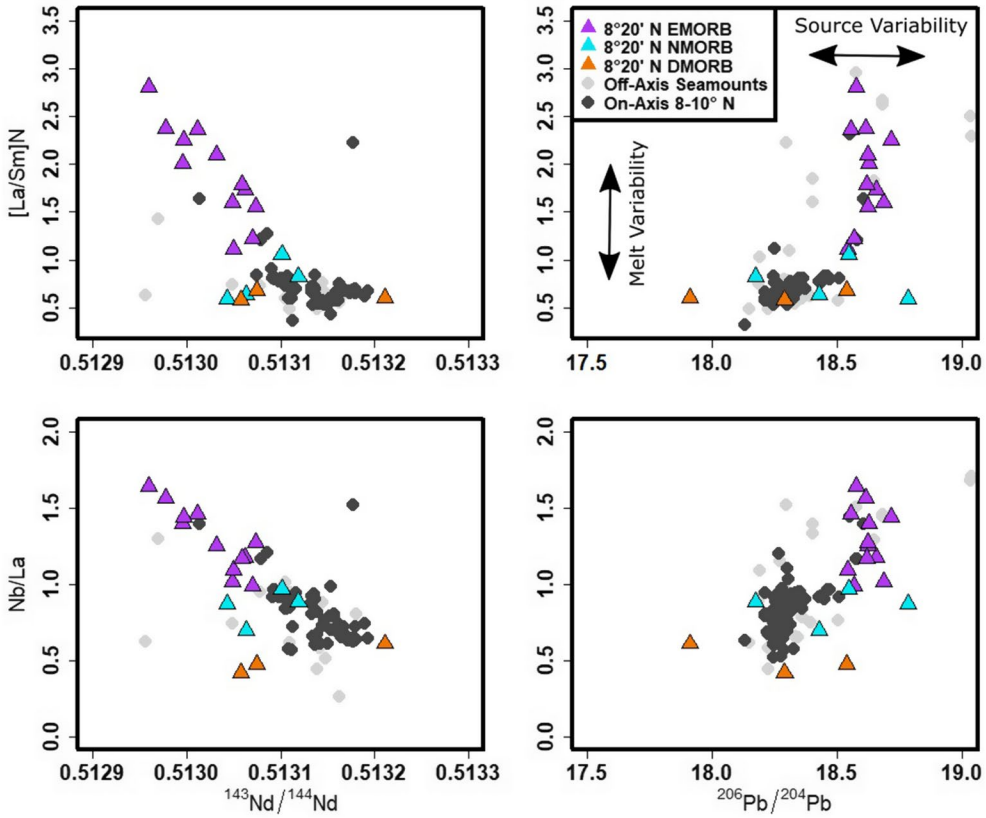

Figure 10. Radiogenic isotope compositions and incompatible trace element ratios for the 8°20′N seamount lavas compared with on-axis basalts (black circles) and off-axis seamount basalts from the literature not included in this study (gray circles). Radiogenic isotope compositions compared to incompatible trace element ratios show general correlations between LREE enrichment $[La/Sm]_N$ in EMORB and more radiogenic Nd and Pb, but only slightly in D- and NMORB. The effects of variable extents of melting and source variability shown by the arrows suggest both have been present in the origin of the seamount lavas. The similarities in NMORB from both the EPR axial basalts and seamount NMORB reflect the similarity of sources and processes that are operative beneath the seamounts.

at 8˚20′N (EMM and DDMM), we compared radiogenic isotope ratios (Pb, Sr, and Nd) with ratios of trace elements sharing common distribution coefficients (i.e., Nb/La vs. $^{143}Nd/^{144}Nd$ ratios; Figure 10). Based on this, trace element contents for the end-member components in the petrologic models were adjusted slightly from reported EMM and DDMM in the literature (Donnelly et al., 2004; Workman & Hart, 2005) to more closely match local end-members of the seamount lavas (S9). The new trace element concentrations for each component were mixed in 10% increments to produce a suite of source compositions, which were subsequently melted using alphaMELTs (P. M. Smith & Asimow, 2005). Water contents for starting compositions, based on H_2O/Ce ratios of 112 and 200, respectively (Kovalenko et al., 2006; Michael, 1995; Saal et al., 2002; Workman & Hart, 2005), were 100 ppm for DDMM and 400 ppm for EMM, and concentrations between these values for intermediate mixtures. Melting models were run using isentropic, polybaric melting starting between 30 and 40 kbar and at 1300°C and 1400°C; however, the best-fit models were consistently 1,400°C and 40 kbar.

Using the two-component lherzolitic mantle, the entire range of seamount lava compositions can be explained by <1%–15% melting of a heterogeneous mantle composed of mixtures of DDMM and EMM (Figure 11). In general, DMORB lavas are produced by ~5%–15% melting of predominantly DDMM (containing up to 5% EMM). NMORB can be explained by 5%–15% melting of a slightly more enriched mantle than DMORB (~5%–15% EMM). EMORB span a much wider range of melting extents and source variability, ranging from <1% melting of a 10% EMM mantle to >15% melting of up to a 100% EMM mantle. These results suggest that the full range of compositions and elemental ratios in lavas erupted along

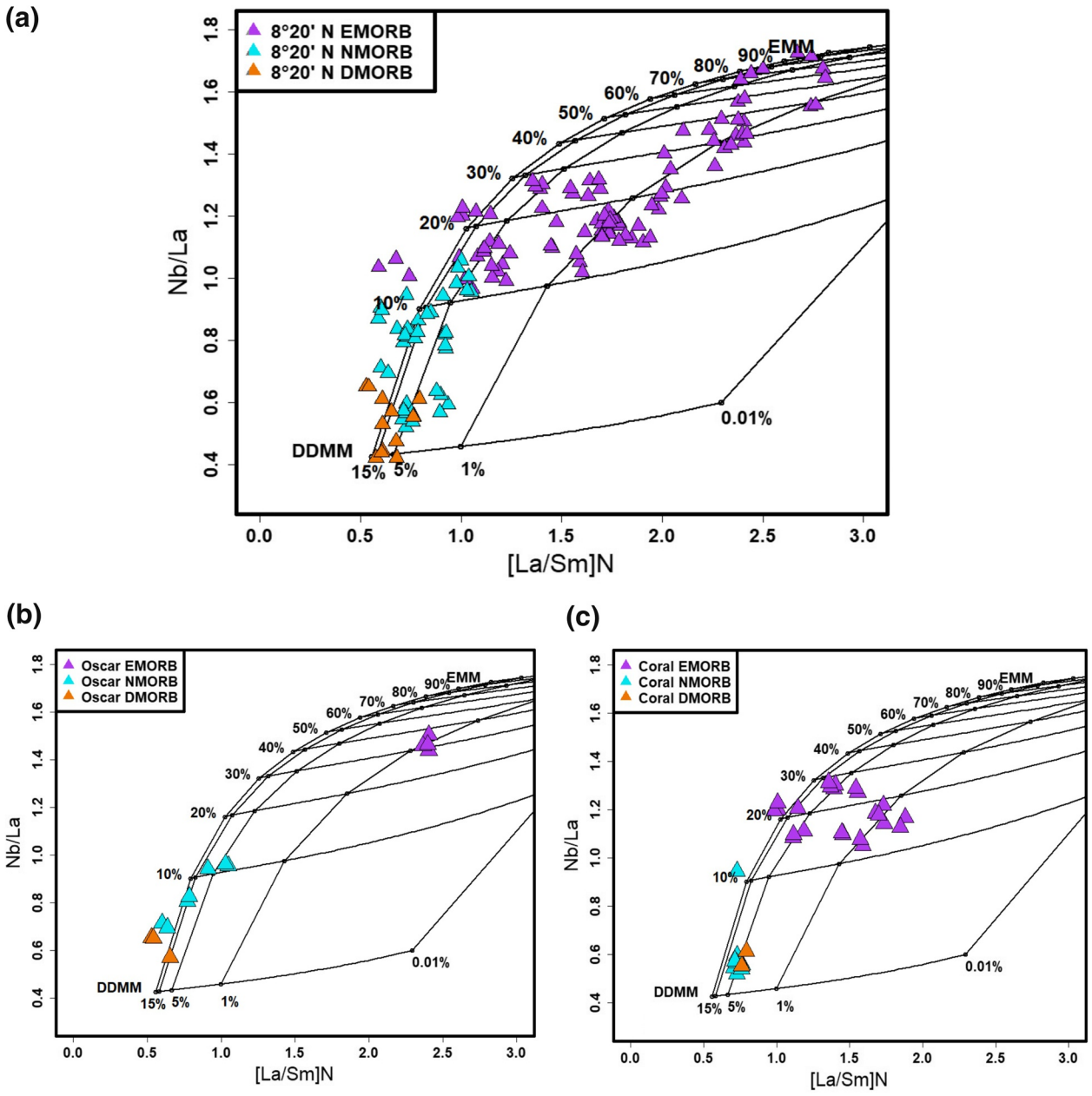

Figure 11. (a) $[La/Sm]_N$ and Nb/La of all 8°20′N seamount lavas characterized by MORB-type. Models for melting change along the *x*-axis ($[La/Sm]_N$ variability) and models for source mixing between a depleted MORB mantle and an enriched MORB mantle change along the *y*-axis (Nb/La variability). Models assume a simple two-component lherzolite system. Horizontal lines represent melting models from compositions of the first melts of each source on the right melted to 15% toward the left. Sub-horizontal lines are incremental mixtures of source compositions DDMM and EMM and sub-vertical lines are tie lines between same melt fractions of different source mixtures, ranging from >0% to 15% melt. The grid demonstrates melting and source conditions that could form each lava by either mixing the mantle sources and then melting those mixtures, or melting each source component, and then mixing those melts in the mantle or crust. (b) $[La/Sm]_N$ and Nb/La of all Oscar seamount lavas compared with the petrologic models. Note how on Oscar seamount, lava compositions span a wide range of source compositions (vertical variability) and melting degree (horizontal variability). (c) $[La/Sm]_N$ and Nb/La of all Coral seamount lavas compared with the petrologic models. At Coral seamount, lava compositions span a wide range of source compositions (vertical variability) and melting degree (horizontal variability). These models indicate that the heterogeneous mantle is melted to variable degrees beneath the seamount chain both along the entire span of the chain, and below individual seamounts sampled in the study area.

the seamount chain are consistent with variable extents of melting of a heterogeneous lherzolitic mantle source (Figure 9). However, it is possible that some variability could be related to a third unaccounted-for enriched source.

5.5. Magmatic Formation of 8°20′N Lava Compositions

An outstanding question regarding the petrogenesis of the 8°20′N seamount chain is the timing of formation. Unfortunately, the ages of the seamounts are unknown at present. However, there are several lines of evidence that suggest the seamounts did not form on-axis. Magnetic polarity differences between the seamounts and the underlying seafloor are consistent with the formation of the seamounts on older oceanic crust away from the ridge axis (Scheirer & Macdonald, 1995), and potentially as far as 100 km from the ridge axis (Romano et al., 2017). The large range of basalt compositions present along the 8°20′N seamount chain as well as their proximity to each other is inconsistent with magmas evolving in well-mixed magma chambers and instead points to independent plumbing systems—unlike those present beneath the EPR axis.

If the seamounts were formed from the vertical ascent of magmas created in the melting triangle directly below each seamount, we would expect a systematic change in the melting extents reflected in lava compositions along the chain (Figure 9). Assuming a constant melt production rate (<1% / 0.1 GPa) within the upwelling region, current models place the highest extents of mantle melting directly beneath the ridge axis with progressively lower extents of melting occurring with greater distance from the ridge axis (Langmuir et al., 1992; O'Hara, 1985; Plank & Langmuir, 1992). This change in total extent of melting from the center of the melting triangle to its wings theoretically results in variable magma compositions due to the relative incompatibilities of trace elements; higher extents of melting produce depleted incompatible trace element ratios and lower extents of melting lead to enriched trace element ratios. However, no systematic change in lava composition is observed with distance from the ridge axis (Figure 8). In fact, nearly the entire range of MORB compositions in the northeast Pacific can be found on individual seamounts. Furthermore, there is no change in composition with depth on the seamount edifice, suggesting that lava compositions have not changed systematically with time.

The wide range of lavas recovered from individual seamounts suggest that melting systematics and mantle sources are variable on small spatial scales, a finding not unique to the 8°20′N seamount chain (e.g., Brandl et al., 2012; Gill et al., 2016; Niu et al., 2002, Figure 9). This range of compositional variability is even observed near the ridge axis (Figure 8). A combination of variable extents of melting and source variability is required to explain the range of compositions erupted on this seamount (Figure 11), suggesting that variability in these petrologic processes and sources occur over short length and timescales. This supports our contention that EMM and DDMM mantle components are present in the sub-ridge mantle (Figure 9), but their end-member signatures are diminished by large extents of melting and focusing beneath the ridge crest and are overprinted by mixing in on-axis magma chambers.

Combined, these observations suggest that the seamount lavas are not formed by systematically tapping different portions of the MOR melting triangle, as simpler models might predict. Instead, these models suggest that the 8°20′N seamount chain formed from variable extents of melting of a heterogeneous mantle that spans the range of compositions inferred to exist in the northern EPR region.

6. Conclusion

Geochemical studies of MORB recovered from the axial regions of fast-spreading ridges provide only limited information about the mantle from which they were derived due to efficient mixing and homogenization of magmas in sub-axial melt lenses and across the entire melting region prior to eruption. The unique location and orientation of the near-axis 8°20′N seamount chain provides an opportunity for detailed spatial investigations of mantle heterogeneity and melting systematics near a fast-spreading MOR without the obscuring effects of long-term magma focusing and mixing along the ridge axis.

The 8°20′N seamount lavas exceed the compositional range of major and trace elements and radiogenic isotopes of on-axis lavas, and instead are similar to the full compositional range of northeast Pacific non-hotspot basalts. This suggests that the EMM and DDMM mantle components are present in the sub-ridge mantle, but are often overprinted at the ridge by mixing in on-axis magma chambers.

Based on geochemistry and petrologic modeling, mixtures of both very depleted (DDMM) and enriched mantle (EMM) sources melted to variable degrees are required to explain the lavas erupted on the seamounts. Generally, DMORB lavas are produced by ~5%–15% melting of DDMM, with the exception of one DMORB sample with elevated Nd isotopes. NMORB can be explained by 5%–15% melting of a slightly more

enriched mantle than DMORB (~5%–15% EMM). EMORB vary greatly from <1% melting of a 10% EMM mantle to >15% melting of up to a 100% EMM mantle. These are mixed at all locations along the chain.

Almost the entire range of compositions is observed on the summit of Oscar seamount, closest to the ridge axis, suggesting that both mantle components are present and can be preserved very near to the ridge axis. Thus, the distinct mantle sources from which the lavas were derived must exist over small (<1 km) spatial scales, and the sub-seamount plumbing systems must remain separated from the on-axis system to avoid mixing and homogenization.

Data Availability Statement

Data in support of this manuscript are available online at EarthChem https://doi.org/10.26022/IEDA/111616.

Acknowledgments
The authors are grateful to the captain and crew of the *R/V Atlantis* (AT37-05), pilots of HOV *Alvin* and the whole AUV *Sentry* support team who were key to our successful field operations. They are also thankful to other members of the OASIS (Off-Axis Seamount Investigation at Siqueiros) Expedition Science Team that included M. Smith, D. Geist, S. Shirey, C. Lundstrom, H. Cabaniss, B. Boulahanis, E. McCully, C. Trim, V. Romano, Y.J. Tan, J. Albright, and Y. Zhan. Analytical assistance from M. Lytle, K. Bermudez, and G. Kamenov was invaluable and greatly appreciated. They thank E. Todd, Y. Niu, E. Klein, and one anonymous reviewer for their insightful comments which greatly improved the manuscript, and R. Russo for assistance using GMT. This work was supported by NSF OCE-MGG 1356610 (Romano and Gregg), NSF OCE-MGG 1356822 (Fornari), NSF OCE-MGG 1357150 (Perfit), NSF OCE-MGG 2001314 (Perfit and Wanless), the Burnham Research Grant at Boise State University, and the Graduate School Funding Fellowship at University of Florida.

References

Allan, J. F., & Batiza, R. (1987). *Petrology and chemistry of lavas from seamounts flanking the East Pacific Rise axis, 21 N: Implications concerning the mantle source composition for both seamount and adjacent EPR lavas* (pp. 255–282). American Geophysical Union Monogram Series.

Allan, J. F., Perfit, M. R., Fornari, D. J., & Sack, R. O. (1989). Petrology of lavas from the Lamont seamount chain and adjacent East Pacific Rise, 10 N. *Journal of Petrology*, *30*(5), 1245–1298.Retrieved from https://doi-org.lp.hscl.ufl.edu/10.1093/petrology/30.5.1245

Arevalo, R., & McDonough, W. F. (2010). Chemical variations and regional diversity observed in MORB. *Chemical Geology*, *271*(1–2), 70–85. https://doi.org/10.1016/j.chemgeo.2009.12.013

Batiza, R., & Niu, Y. (1992). Petrology and magma chamber processes at the East Pacific Rise ~9°30'N. *Journal of Geophysical Research*, *97*(B5), 6779–6797.

Batiza, R., Niu, Y., Karsten, J., Boger, W., Potts, E., Norby, L., et al. (1996). Steady and non-steady state magma chambers below the East Pacific Rise. *Geophysical Research Letters*, *23*(3), 221–224. https://doi.org/10.1029/95GL00016

Batiza, R., Niu, Y., & Zayac, W. C. (1990). Chemistry of seamounts near the East Pacific Rise: Implications for the geometry of subaxial mantle flow. *Geology*, *18*(11), 1122–1125. https://doi.org/10.1130/0091-7613(1990)018<1122:COSNTE>2.3.CO;2

Batiza, R., Smith, T. L., & Niu, Y. (1989). Geological and petrologic evolution of seamounts near the EPR based on submersible and camera study. *Marine Geophysical Researches*, *11*(3), 169–236. https://doi.org/10.1007/BF00340203

Batiza, R., & Vanko, D. (1984). Petrology of young Pacific seamounts. *Journal of Geophysical Research*, *89*(B13), 11235–11260. https://doi.org/10.1029/JB089iB13p11235

Behn, M. D., & Grove, T. L. (2015). Melting systematics in mid-ocean ridge basalts: Application of a plagioclase-spinel melting model to global variations in major element chemistry and crustal thickness. *Journal of Geophysical Research: Solid Earth*, *120*, 4863–4886. https://doi.org/10.1002/2015JB012608

Behn, M. D., Lin, J., & Zuber, M. T. (2002). Evidence for weak oceanic transform faults. *Geophysical Research Letters*, *29*(24), 1–4. https://doi.org/10.1029/2002GL015612

Bo, T., Katz, R. F., Shorttle, O., & Rudge, J. F. (2018). The melting column as a filter of mantle trace-element heterogeneity. *Geochemistry, Geophysics, Geosystems*, *19*(12), 4694–4721. https://doi.org/10.1029/2018GC007880

Boudier, F., & Coleman, R. G. (1981). Cross section through the peridotite in the Samail Ophiolite, southeastern Oman Mountains. *Journal of Geophysical Research*, *86*(B4), 2573–2592. https://doi.org/10.1029/JB086iB04p02573

Brandl, P. A., Beier, C., Regelous, M., Abouchami, W., Haase, K. M., Garbe-Schonberg, D., et al. (2012). Volcanism on the flanks of the East Pacific Rise: Quantitative constraints on mantle heterogeneity and melting processes. *Chemical Geology*, *298–299*, 41–56. https://doi.org/10.1016/j.chemgeo.2011.12.015

Carbotte, S. M., Arko, R., Chayes, D. N., Haxby, W., Lehnert, K., O'Hara, S., et al. (2004). New integrated data management system for Ridge2000 and MARGINS research. *Eos, Transactions American Geophysical Union*, *85*(51), 553. https://doi.org/10.1029/2004EO510002

Carbotte, S., & Macdonald, K. (1992). East Pacific Rise 8°–10°30′N: Evolution of ridge segments and discontinuities from SeaMARC II and three-dimensional magnetic studies. *Journal of Geophysical Research*, *97*(B5), 6959. https://doi.org/10.1029/91JB03065

Carmichael, I. S. E., Turner, F. J., & Verhoogen, J. (1974). *Igneous petrology*. New York, London: McGraw-Hill.

Clague, D. A., Reynolds, J. R., & Davis, A. S. (2000). Near-ridge seamount chains in the northeastern Pacific Ocean. *Journal of Geophysical Research*, *105*(B7), 16541–16561. https://doi.org/10.1029/2000jb900082

Conrad, E. M., Perfit, M. R., Anderson, M., Wanless, V. D., Fornari, D. J., & Gregg, P. M. (2018). *Geochemical diversity of lavas from the 8°20′ N seamount chain provides insights into seamount evolution from a heterogeneous mantle. Abstract V43G-0199 at 2018 Fall Meeting*. Washington, DC: AGU.

Cottrell, E., & Kelley, K. (2013). Redox heterogeneity in mid-ocean ridge basalts as a function of mantle source. *Science*, *340*, 1314–1318.

Coumans, J. P., Stix, J., Clague, D. A., & Minarik, W. G. (2015). The magmatic architecture of Taney seamount-A, NE Pacific Ocean. *Journal of Petrology*, *56*(6), 1037–1067. https://doi.org/10.1093/petrology/egv027

Davis, A. S., & Clague, D. A. (2000). President Jackson Seamounts, northern Gorda Ridge: Tectonomagmatic relationship between on- and off-axis volcanism. *Journal of Geophysical Research*, *105*(B12), 27939–27956. https://doi.org/10.1029/2000jb900291

Davis, E. E., & Karsten, J. L. (1986). On the cause of the asymmetric distribution of seamounts about the Juan de Fuca ridge: Ridge-crest migration over a heterogeneous asthenosphere. *Earth and Planetary Science Letters*, *79*(3–4), 385–396.

Donnelly, K. E., Goldstein, S. L., Langmuir, C. H., & Spiegelman, M. (2004). Origin of enriched ocean ridge basalts and implications for mantle dynamics. *Earth and Planetary Science Letters*, *226*(3–4), 347–366. https://doi.org/10.1016/j.epsl.2004.07.019

Edwards, M. H., Fornari, D. J., Malinverno, A., Ryan, W. B. F., & Madsen, J. (1991). The regional tectonic fabric of the East Pacific Rise from 12°50'N to 15°10'N. *Journal of Geophysical Research*, *96*(B5), 7995–8017. https://doi.org/10.1029/91JB00283

Fabbrizzi, A., Parnell-Turner, R., Gregg, P., Fornari, D., Perfit, M., Wanless, V. D., et al. (2020). Dating Off-Axis Volcanism Along the 8°20'N Seamount Chain Using Sediment Thickness Proxy from Near-bottom Chirp Images. *American geophysical union fall meeting. Virtual online: American geophysical union*.

Fornari, D. J., Gallo, D. G., Edwards, M. H., Madsen, J. A., Perfit, M. R., & Shor, A. N. (1989). Structure and topography of the Siqueiros transform fault system: Evidence for the development of intra-transform spreading centers. *Marine Geophysical Researches*, *11*(4), 263–299.

Fornari, D. J., Perfit, M. R., Allan, J. F., & Batiza, R. (1988a). Small-scale heterogeneities in depleted mantle sources: Near-ridge seamount lava geochemistry and implications for mid-ocean-ridge magmatic processes. *Nature*, *331*, 511–513. https://doi.org/10.1038/332141a0

Fornari, D. J., Perfit, M. R., Allan, J. F., Batiza, R., Haymon, R., Barone, A., et al. (1988b). Geochemical and structural studies of the Lamont seamounts: seamounts as indicators of mantle processes. *Earth and Planetary Science Letters*, *89*(1), 63–83. https://doi.org/10.1016/0012-821X(88)90033-7

Forsyth, D. W., Scheirer, D. S., Webb, S. C., Dorman, L. M., Orcutt, J. A., Harding, A. J., et al. (1998). Imaging the deep seismic structure beneath a mid-ocean ridge: The MELT experiment: The MELT seismic team. *Science*, *280*(5367), 1215–1218. https://doi.org/10.1126/science.280.5367.1215

Gale, A., Dalton, C., Langmuir, C. H., Su, Y., & Schilling, J. G. (2013). The mean composition of ocean ridge basalts. *Geochemistry, Geophysics, Geosystems*, *14*(3), 489–518.

Gill, J., Michael, P., Woodcock, J., Dreyer, B., Ramos, F., Clague, D., et al. (2016). Spatial and temporal scale of mantle enrichment at the Endeavor Segment, Juan de Fuca Ridge. *Journal of Petrology*, *57*(5), 863–896.

Gleeson, M. L., Gibson, S. A., & Williams, H. M. (2020). Novel insights from the Fe-isotopes into the lithological heterogeneity of Ocean Island Basalts and plume-influenced MORBs. *Earth and Planetary Science Letters*, *535*, 116114.

Goff, J. A., Malinverno, A., Fornari, D. J., & Cochran, J. R. (1993). Abyssal hill segmentation: Quantitative analysis of the East Pacific Rise flanks 7°S–9°S. *Journal of Geophysical Research*, *98*(B8), 13851–13862. https://doi.org/10.1029/93JB01095

Goss, A. R., Perfit, M. R., Ridley, W. I., Rubin, K. H., Kamenov, G. D., Soule, S. A., et al. (2010). Geochemistry of lavas from the 2005-2006 eruption at the East Pacific Rise, 9°46'N-9°56N: Implications for ridge crest plumbing and decadal changes in magma chamber compositions. *Geochemistry, Geophysics, Geosystems*, *11*(5), 1–35. https://doi.org/10.1029/2009GC002977

Gregg, P. M., Behn, M. D., Lin, J., & Grove, T. L. (2009). Melt generation, crystallization, and extraction beneath segmented oceanic transform faults. *Journal of Geophysical Research*, *114*(11). https://doi.org/10.1029/2008JB006100

Gregg, P. M., Montesi, L. G. J., & Katz, R. F. (2012). Geodynamic models of melt generation and extraction at mid-ocean ridges. *Oceanography*, *25*(3), 56–67. https://doi.org/10.5670/oceanog.2011.65

Hebert, L. B., & Montési, L. G. J. (2010). Generation of permeability barriers during melt extraction at mid-ocean ridges. *Geochemistry, Geophysics, Geosystems*, *11*(12), 1–17. https://doi.org/10.1029/2010GC003270

Hebert, L. B., & Montési, L. G. (2011). Melt extraction pathways at segmented oceanic ridges: Application to the East Pacific Rise at the Siqueiros transform. *Geophysical Research Letters*, *38*(11). https://doi.org/10.1029/2011GL047206

Hirschmann, M. M., & Stolper, E. M. (1996). A possible role for garnet pyroxenite in the origin of the "garnet signature" in MORB. *Contributions to Mineralogy and Petrology*, *124*, 185–208.Retrieved from http://dx.doi.org/10.1007/s004100050184

Hofmann, A. W. (1997). Mantle geochemistry: the message from oceanic volcanism. *Nature*, *385*, 219–229.

Kamenov, G., Perfit, M., Mueller, P., & Jonasson, I. (2008). Controls on magmatism in an island arc environment: Study of lavas and sub-arc xenoliths from the Tabar-Lihir-Tanga-Feni island chain, Papua New Guinea. *Contributions to Mineralogy and Petrology*, *155*(5), 635–656.

Katz, R. F. (2008). Magma dynamics with the enthalpy method: Benchmark solutions and magmatic focusing at mid-ocean ridges. *Journal of Petrology*, *49*(12), 2099–2121. https://doi.org/10.1093/petrology/egn058

Katz, R. F., & Weatherley, S. M. (2012). Consequences of mantle heterogeneity for melt extraction at mid-ocean ridges. *Earth and Planetary Science Letters*, *335*(336), 226–237. https://doi.org/10.1016/j.epsl.2012.04.042

Keller, T., Katz, R. F., & Hirschmann, M. M. (2017). Volatiles beneath mid-ocean ridges: Deep melting, channelised transport, focusing, and metasomatism. *Earth and Planetary Science Letters*, *464*, 55–68. https://doi.org/10.1016/j.epsl.2017.02.006

Key, K., Constable, S., Liu, L., & Pommier, A. (2013). Electrical image of passive mantle upwelling beneath the northern East Pacific Rise. *Nature*, *495*(7442), 499–502. https://doi.org/10.1038/nature11932

Kovalenko, V. I., Naumov, V. B., Girnis, A. V., Dorofeeva, V. A., & Yarmolyuk, V. V. (2006). Estimation of the average contents of H2O, Cl, F, and S in the depleted mantle on the basis of the compositions of melt inclusions and quenched glasses of mid-ocean ridge basalts. *Geochemistry International*, *44*(3), 209–231. https://doi.org/10.1134/s0016702906030013

Langmuir, C., Klein, E., & Plank, T. (1992). Petrological systematics of mid-ocean ridge basalts: Constraints on melt generation beneath ocean ridges. *American Geophysical Union*, *71*, 183–279.

le Roux, P. J., Shirey, S. B., Hauri, E. H., Perfit, M. R., & Bender, J. F. (2006). The effects of variable sources, processes and contaminants on the composition of northern EPR MORB (8-10°N and 12-14°N): Evidence from volatiles (H2O, CO2, S) and halogens (F, Cl). *Earth and Planetary Science Letters*, *251*(3–4), 209–231. https://doi.org/10.1016/j.epsl.2006.09.012

Lundstrom, C. C., Sampson, D. E., Perfit, M. R., Gill, J., & Williams, Q. (1999). Insights into mid-ocean ridge basalt petrogenesis: U-series disequilibria from the Siqueiros Transform, Lamont Seamounts, and East Pacific Rise. *Journal of Geophysical Research*, *104*(B6), 13035–13048. https://doi.org/10.1029/1999jb900081

Macdonald, K. C., Fox, P. J., Miller, S., Carbotte, S., Edwards, M. H., Eisen, M., et al. (1992). The East Pacific Rise and its flanks 8–18 N: History of segmentation, propagation and spreading direction based on SeaMARC II and Sea Beam studies. *Marine Geophysical Researches*, *14*(4), 299–344.

Mallick, S., Salters, V. J. M., & Langmuir, C. H. (2019). Geochemical variability along the northern East Pacific Rise: Coincident source composition and ridge segmentation. *Geochemistry, Geophysics, Geosystems*, *20*, 1–23. https://doi.org/10.1029/2019GC008287

Mallick, S., Standish, J. J., & Bizimis, M. (2015). Constraints on the mantle mineralogy of an ultra-slow ridge: Hafnium isotopes in abyssal peridotites and basalts from the 9–25°E Southwest Indian Ridge. *Earth and Planetary Science Letters*, *410*, 42–53. https://doi.org/10.1016/j.epsl.2014.10.048

Mckenzie, D., & Bickle, M. J. (1988). The volume and composition of melt generated by extension of the lithosphere. *Journal of Petrology*, *29*(3), 625–679. https://doi.org/10.1093/petrology/29.3.625

McKenzie, D., Stracke, A., Blichert-Toft, J., Albarède, F., Grönvold, K., & O'Nions, R. K. (2004). Source enrichment processes responsible for isotopic anomalies in oceanic island basalts. *Geochimica et Cosmochimica Acta*, *68*(12), 2699–2724. https://doi.org/10.1016/j.gca.2003.10.029

Michael, P. (1995). Regionally distinctive sources of depleted MORB: Evidence from trace elements and H2O. *Earth and Planetary Science Letters*, *131*(3–4), 301–320. https://doi.org/10.1016/0012-821X(95)00023-6

Niu, Y. (1997). Mantle melting and melt extraction processes beneath ocean ridges: Evidence from abyssal peridotites. *Journal of Petrology*, *38*(8), 1047–1074.
Niu, Y., & Batiza, R. (1997a). Extreme mantle source heterogeneities beneath the northern East Pacific Rise: Trace element evidence from near-ridge seamounts. *International Geological Congress, 30th, Proceedings*, *15*, 109–120.
Niu, Y., & Batiza, R. (1997). Trace element evidence from seamounts for recycled oceanic crust in the Eastern Pacific mantle. *Earth and Planetary Science Letters*, *148*(3), 471–483. https://doi.org/10.1016/S0012-821X(97)00048-4
Niu, Y., Collerson, K. D., Batiza, R., Wendt, I. J., & Regelous, M. (1999). Origin of enriched-type mid-ocean ridge basalt at ridges far from mantle plumes: The East Pacific Rise at 11°20′N. *Journal of Geophysical Research*, *104*(B4), 7067–7087. https://doi.org/10.1029/1998JB900037
Niu, Y., & Hekinian, R. (2004). Ridge suction drives plume-ridge interactions (Chapter 9). In R. Hekinian, & P. Stoffers (Eds.), *Oceanic hotspots* (pp. 285–307). New York: Springer-Verlag.
Niu, Y., Regelous, M., Wendt, I. J., Batiza, R., & O'Hara, M. J. (2002). Geochemistry of near-EPR seamounts: Importance of source vs. process and the origin of enriched mantle component. *Earth and Planetary Science Letters*, *199*(3–4), 327–345. https://doi.org/10.1016/S0012-821X(02)00591-5
Niu, Y., Waggoner, D. G., Sinton, J. M., & Mahoney, J. (1996). Mantle source heterogeneity and melting processes beneath seafloor spreading centers: The East Pacific Rise, 18–19 S. *Journal of Geophysical Research*, *101*(B12) 27711–27733. https://doi.org/10.1029/96JB01923
Niu, Y., Wilson, M., Humphreys, E., & O'Hara, M. J. (2012). A trace element perspective on the source of ocean island basalts (OIB) and fate of subducted ocean crust (SOC) and mantle lithosphere (SML). *Episodes*, *35*(2), 310–327.
O'Hara, M. J. (1985). Importance of the "shape" of the melting regime during partial melting of the mantle. *Nature*, *314*, 58–62.
Perfit, M., Fornari, D. J., Ridley, W. I., Kirk, P. D., Casey, J., Kastens, K. A., et al. (1996). Recent volcanism in the Siqueiros transform fault: Picritic basalts and implications for MORB magma genesis. *Earth and Planetary Science Letters*, *141*, 91–108. https://doi.org/10.1016/0012-821X(96)00052-0
Perfit, M., Fornari, D. J., Smith, M. C., Bender, J. F., Langmuir, C. H., & Haymon, R. M. (1994). Small-scale spatial and temporal variations in mid-ocean ridge crest magmatic processes. *Geology*, *22*(4), 375–379.
Perfit, M., Smith, R., Walters, R., Ridley, W. I., & Fornari, D. J. (2013). *Compilation of east Pacific 9 Deg–10 Deg N basalt geochemistry*. EarthChem Library.
Perfit, M., Wanless, V. D., Ridley, W. I., Klein, E., Smith, M., Goss, A., et al. (2012). Lava geochemistry as a probe into crustal formation at the East Pacific Rise. *Oceanography*, *25*(1), 89–93. https://doi.org/10.5670/oceanog.2012.06
Phipps-Morgan, J. (1987). Melt migration beneath mid-ocean spreading centers. *Geophysical Research Letters*, *14*(12), 1238–1241. https://doi.org/10.1029/GL014i012p01238
Pilet, S., Baker, M., Muntener, O., & Stolper, E. (2011). Monte Carlo simulations of metasomatic enrichment in the lithosphere and implications for the source of alkaline basalts. *Journal of Petrology*, *52*(7–8), 1415–1442.
Pilet, S., Baker, M., & Stolper, E. (2008). Metasomatized lithosphere and the origin of alkaline lavas. *Science*, *320*(5878), 916–919.
Plank, T., & Langmuir, C. H. (1992). Effects of the melting regime on the composition of the oceanic crust. *Journal of Geophysical Research*, *97*(B13), 19749–19770. https://doi.org/10.1029/92JB01769
Pockalny, R. A., Fox, P. J., Fornari, D. J., Macdonald, K. C., & Perfit, M. R. (1997). Tectonic reconstruction of the Clipperton and Siqueiros Fracture Zones: Evidence and consequences of plate motion change for the last 3 Myr. *Journal of Geophysical Research*, *102*(B2), 3167–3181. https://doi.org/10.1029/96jb03391
Reynolds, J. R., & Langmuir, C. H. (2000). Identification and implications of off-axis lava flows around the East Pacific Rise. *Geochemistry, Geophysics, Geosystems*, *1*(6). https://doi.org/10.1029/1999GC000033
Reynolds, J. R., Langmuir, C. H., Bender, J. F., Kastens, K. A., & Ryan, W. B. F. (1992). Spatial and temporal variability in the geochemistry of basalts from the East Pacific Rise. *Nature*, *359*, 493–499.
Romano, V., Gregg, P., Zhan, Y., Fornari, D., Perfit, M., & Battaglia, M. (2017). *Formation and evolution of the near Axis 8°20′ N seamount chain: Evidences from the geophysical data analysis*. New Orleans, LA: American Geophysical Union Fall Meeting. American Geophysical Union.
Rubin, K. H., & Sinton, J. M. (2007). Inferences on mid-ocean ridge thermal and magmatic structure from MORB compositions. *Earth and Planetary Science Letters*, *260*(1–2), 257–276 https://doi.org/10.1016/j.epsl.2007.05.035
Rubin, K. H., Sinton, J. M., MacLennan, J., & Hellebrand, E. (2009). Magmatic filtering of mantle compositions at mid-ocean-ridge volcanoes. *Nature Geoscience*, *2*(5), 321–328. https://doi.org/10.1038/ngeo504
Saal, A. E., Hauri, E. H., Langmuir, C. H., Perfit, M. R. (2002). Vapour undersaturation in primitive mid-ocean-ridge basalt and the volatile content of Earth's upper mantle. *Nature*, *419*, (6906), 451–455. http://dx.doi.org/10.1038/nature01073
Scheirer, D. S., & Macdonald, K. C. (1995). Near-axis seamounts on the flanks of the East Pacific Rise, 8°N to 17°N. *Journal of Geophysical Research*, *100*(B2), 2239–2259. https://doi.org/10.1029/94JB02769
Shimizu, K., Saal, A. E., Myers, C. E., Nagle, A. N., Hauri, E. H., Forsyth, D. W., et al. (2016). Two-component mantle melting-mixing model for the generation of mid-ocean ridge basalts: Implications for the volatile content of the Pacific upper mantle. *Geochimica et Cosmochimica Acta*, *176*, 44–80. https://doi.org/10.1016/j.gca.2015.10.033
Sims, K. W., Goldstein, S., Blichert-toft, J., Perfit, M., Kelemen, P., Fornari, D., & Bender, J. (2002). Chemical and isotopic constraints on the generation and transport of magma beneath the East Pacific Rise. *Geochimica et Cosmochimica Acta*, *66*(19), 3481–3504. https://doi.org/10.1016/S0016-7037(02)00909-2
Sinton, J. M., & Detrick, R. S. (1992). Mid-ocean ridge magma chambers. *Journal of Geophysical Research*, *97*(B1), 197–213. https://doi.org/10.1029/91JB02508
Sinton, J. M., Smaglik, S. M., & Mahoney, J. J. (1991). Magmatic processes at superfast spreading mid-ocean ridges: glass compositional variations along the East Pacific Rise 13°-23°S. *Journal of Geophysical Research*, *96*(B4), 6133–6155. https://doi.org/10.1029/90JB02454
Smith, P. M., & Asimow, P. D. (2005). Adiabat-1ph: A new public front-end to the MELTS, pMELTS, and pHMELTS models. *Geochemistry, Geophysics, Geosystems*, *6*(1). https://doi.org/10.1029/2004GC000816
Smith, M. C., Perfit, M. R., Fornari, D. J., Ridley, W. I., Edwards, M. H., Kurras, G. J., et al. (2001). Magmatic processes and segmentation at a fast spreading mid-ocean ridge: Detailed investigation of an axial discontinuity on the East Pacific Rise crest at 9°37′N. *Geochemistry, Geophysics, Geosystems*, *2*. https://doi.org/10.1029/2000GC000134
Sobolev, A. V., Hofmann, A. W., Kuzmin, D. V., Yaxley, G. M., Arndt, N. T., Chung, S. L., et al. (2007). The amount of recycled crust in sources of mantle-derived melts. *Science*, *316*, 412–417.
Sparks, D. W., & Parmentier, E. M. (1991). Melt extraction from the mantle beneath spreading centers. *Earth and Planetary Science Letters*, *105*(4), 368–377. https://doi.org/10.1016/0012-821X(91)90178-K

Spiegelman, M., & McKenzie, D. (1987). Simple 2-D models for melt extraction at mid-ocean ridges and island arcs. *Earth and Planetary Science Letters*, *83*(1–4), 137–152. https://doi.org/10.1016/0012-821X(87)90057-4

Stracke, A., & Bourdon, B. (2009). The importance of melt extraction for tracing mantle heterogeneity. *Geochimica et Cosmochimica Acta*, *73*(1), 218–238. https://doi.org/10.1016/j.gca.2008.10.015

Stracke, A., Salters, V. J. M., & Sims, K. W. W. (1999). Assessing the presence of garnet-pyroxenite in the mantle sources of basalts through combined hafnium-neodymium-thorium isotope systematics. *Geochemistry, Geophysics, Geosystems*, *1*(12). https://doi.org/10.1029/1999GC000013

Sun, P., & McDonough, W. (1989). Chemical and isotopic systematics of oceanic basalts: Implications for mantle composition and processes. *Geological Society, London, Special Publications*, *42*, 313–345. https://doi.org/10.1144/gsl.sp.1989.042.01.19

Sun, P., Niu, Y., Guo, P., Duan, M., Chen, S., Gong, H., et al. (2020). Large iron isotope variation in the eastern Pacific mantle as a consequence of ancient low-degree melt metasomatism. *Geochimica et Cosmochimica Acta*, *286*, 269–288. https://doi.org/10.1016/j.gca.2020.07.029

Turner, A. J., Katz, R. F., Behn, M. D., & Keller, T. (2017). Magmatic focusing to mid-ocean ridges: the role of grain-size variability and non-Newtonian viscosity. *Geochemistry, Geophysics, Geosystems*, *18*(12), 4342–4355. https://doi.org/10.1002/2017GC007048

Wanless, V. D., Behn, M. D., Shaw, A. M., & Plank, T. (2014). Variations in melting dynamics and mantle compositions along the Eastern Volcanic Zone of the Gakkel Ridge: Insights from olivine-hosted melt inclusions. *Contributions to Mineralogy and Petrology*, *167*(5), 1–22. https://doi.org/10.1007/s00410-014-1005-7

Wanless, V. D., Perfit, M. R., Klein, E. M., White, S., & Ridley, W. I. (2012). Reconciling geochemical and geophysical observations of magma supply and melt distribution at the 9°N overlapping spreading center, East Pacific Rise. *Geochemistry, Geophysics, Geosystems*, *13*(11), 1–22. https://doi.org/10.1029/2012GC004168

Wanless, V. D., Perfit, M. R., Ridley, W. I., Wallace, P., Grimes, C. B., & Klein, E. M. (2011). Volatile abundances and oxygen isotopes in basaltic to dacitic lavas on mid-ocean ridges: The role of assimilation at spreading centers. *Chemical Geology*, *287*, 54–65. https://doi.org/10.1016/j.chemgeo.2011.05.017

Wanless, V. D., & Shaw, A. M. (2012). Lower crustal crystallization and melt evolution at mid-ocean ridges. *Nature Geoscience*, *5*(9), 651–655. https://doi.org/10.1038/ngeo1552

Waters, C. L., Sims, K. W. W., Perfit, M. R., Blichert-Toft, J., & Blusztajn, J. (2011). Perspective on the genesis of E-MORB from chemical and isotopic heterogeneity at 9-10°N East Pacific Rise. *Journal of Petrology*, *52*(3), 565–602. https://doi.org/10.1093/petrology/egq091

Workman, R. K., & Hart, S. R. (2005). Major and trace element composition of the depleted MORB mantle (DMM). *Earth and Planetary Science Letters*, *231*(1–2), 53–72. https://doi.org/10.1016/j.epsl.2004.12.005

Workman, R. K., Hart, S. R., Jackson, M., Regelous, M., Farley, K. A., Blusztajn, J., et al. (2004). Recycled metasomatized lithosphere as the origin of the Enriched Mantle II (EM2) end-member: Evidence from the Samoan Volcanic Chain. *Geochemistry, Geophysics, Geosystems*, *5*(4), 1–44. https://doi.org/10.1029/2003GC000623

Yang, S., Humayun, M., & Salters, V. J. (2020). Elemental constraints on the amount of recycled crust in the generation of mid-oceanic ridge basalts (MORBs). *Science Advances*, *6*(26), eaba2923.

Zhang, G.-L., Zong, C.-L., Yin, X.-B., & Li, H. (2012). Geochemical constraints on a mixed pyroxenite-peridotite source for East Pacific Rise basalts. *Chemical Geology*, *330–331*, 176–187. https://doi.org/10.1016/j.chemgeo.2012.08.033

Zindler, A., Staudigel, H., & Batiza, R. (1984). Isotope and trace element geochemistry of young Pacific seamounts: Implications for the scale of upper mantle heterogeneity. *Earth and Planetary Science Letters*, *70*(2), 175–195. https://doi.org/10.1016/0012-821X(84)90004-9

References From the Supporting Information

Arevalo, R., & McDonough, W. F. (2008). Tungsten geochemistry and implications for understanding the Earth's interior. *Earth and Planetary Science Letters*, *272*(3–4), 656–665.

Barth, G., Kastens, K., & Klein, E. (1994). The origin of bathymetric highs at ridge-transform intersections: A multi-disciplinary case study at the Clipperton Fracture Zone. *Marine Geophysical Researches*, *16*(1), 1–50.

Batiza, R. (1982). Abundances, distribution and sizes of volcanoes in the Pacific Ocean and implications for the origin of non-hotspot volcanoes. *Earth and Planetary Science Letters*, *60*(2), 195–206. https://doi.org/10.1016/0012-821X(82)90003-6

Chaussidon, M., Sheppard, S., & Michard, A. (1991). Hydrogen, sulfur and neodymium isotope variations in the mantle beneath the EPR at 12 50'N. Stable isotope geochemistry. *A Tribute to Samuel Epstein*, 325–337.

Cottrell, E., & Kelley, K. (2011). The oxidation state of Fe in MORB glasses and the oxygen fugacity of the upper mantle. *Earth and Planetary Science Letters*, *305*(3–4), 270–282.

Danyushevsky, L., Eggins, S., Falloon, T., & Christie, D. (2000). H2O abundance in depleted to moderately enriched mid-ocean ridge magmas; Part I: Incompatible behaviour, implications for mantle storage, and origin of regional variations. *Journal of Petrology*, *41*(8), 1329–1364.

Goldstein, S., Murrell, M., & Williams, R. (1993). 231Pa and 230Th Chronology of Mid-Ocean Ridge Basalts. *Earth and Planetary Science Letters*, *115*, 151–159.

Graham, D., Michael, P., & Rubin, K. (2018). An investigation of mid-ocean ridge degassing using He, CO2, and δ13C variations during the 2005–06 eruption at 9°50′N on the East Pacific Rise. *Earth and Planetary Science Letters*, *504*, 84–93.

Graham, D., Zindler, A., Kurz, M., Jenkins, W. J., Batiza, R., & Staudigel, H. (1988). He, Pb, Sr and Nd isotope constraints on magma genesis and mantle heterogeneity beneath young Pacific seamounts. *Contributions to Mineralogy and Petrology*, *99*(4), 446–463.

Gregg, P. M., Fornari, D. J., Perfit, M. R., Ridley, W. I., & Kurz, M. (2000). Using submarine lava pillars to record mid-ocean ridge eruption dynamics. *Earth and Planetary Science Letters*, *178*(3–4), 195–214.

Hahm, D., Castillo, P., & Hilton, D. (2009). A deep mantle source for high 3He/4He ocean island basalts (OIB) inferred from Pacific near-ridge seamount lavas. *Geophysical Research Letters*, *36*(20), 2–6. https://doi.org/10.1029/2009GL040560

Hekinian, R., Thompson, G., & Bideau, D. (1989). Axial and off-axial heterogeneity of basaltic rocks from the East Pacific Rise at 12°35′N–12°51′N and 11°26′N–11°30′N. *Journal of Geophysical Research*, *94*, 17437–17463. https://doi.org/10.1029/JB094iB12p17437

Jenner, F., & O'Neill, H. (2012). Analysis of 60 elements in 616 ocean floor basaltic glasses. *Geochemistry, Geophysics, Geosystems*, *13*(2). https://doi.org/10.1029/2011GC004009

Kutza, S. (2002). *Petrology and geochemistry of mid-ocean ridge basalts from the east Pacific rise (9°24'to 10°06'N): Implications for off-axis magmatic processes*. Gainesville, FL: Unpublished thesis for the Department of Geological Sciences. University of Florida.

Marschall, H., Wanless, V. D., Shimizu, N., Pogge Von Strandmann, P., Elliott, T., & Monteleone, B. (2017). The boron and lithium isotopic composition of mid-ocean ridge basalts and the mantle. *Geochimica et Cosmochimica Acta*, *207*, 138. https://doi.org/10.1016/j.gca.2017.03.028

McDonough, W.F., Sun, S.-s. (1995). The composition of the Earth. *Chemical Geology*, *120*, (3-4), 223–253. http://dx.doi.org/10.1016/0009-2541(94)00140-4

Melson, W., & O'Hearn, T. (2003). *Smithsonian volcanic glass file: Smithsonian institution of Washington*. EarthChem Library.

Michael, P., & Cornell, W. (1998). Influence of spreading rate and magma supply on crystallization and assimilation beneath mid-ocean ridges: Evidence from chlorine and major element chemistry of mid-ocean ridge basalts. *Journal of Geophysical Research*, *103*, 18325–18356. https://doi.org/10.1029/98JB00791

Moore, A., Coogan, L., Costa, F., & Perfit, M. (2014). Primitive melt replenishment and crystal-mush disaggregation in the weeks preceding the 2005-2006 eruption 9 50′ N, EPR. *Earth and Planetary Science Letters*, *403*, 15–26.

Natland, J. (1989). Partial melting of a lithologically heterogeneous mantle: Inferences from crystallization histories of magnesian abyssal tholeiites form the Siqueiros Fracture Zone. *Geological Society, London, Special Publications*, *42*(1), 41–70.

Pan, Y., & Batiza, R. (2002). Mid-ocean ridge magma chamber processes: Constraints from olivine zonation in lavas from the East Pacific Rise at 9 Deg 30 Min N and 10 Deg 30 Min N. *Journal of Geophysical Research*, *107*(B1), 1–13. https://doi.org/10.1029/2001JB000435

Pan, Y., & Batiza, R. (2003). Magmatic processes under mid-ocean ridges: A detailed, mineralogic study of lavas from East Pacific Rise 9 Deg 30 Min N, 10 Deg 30 Min N, and 11 Deg 20 Min N. *Geochemistry, Geophysics, Geosystems*, *4*(11). https://doi.org/10.1029/2002gc000309

Perfit, M. (2000). *Submitted data set: Major element compositions of basalt glasses from the east Pacific rise, 9 Deg N*. EarthChem Library. https://doi.org/10.1594/IEDA/100442

Perfit, M., & Chadwick, W. (1998). Magmatism at mid-ocean ridges: Constraints from volcanological and geochemical investigations. *Geophysical Monograph Series*, *106*, 59–115. https://doi.org/10.1029/GM106p0059

Prinzhofer, A., Lewin, E., & Allegre, C. (1989). Stochastic melting of the marble cake mantle: Evidence from local study of the East Pacific Rise at 12 50′ N. *Earth and Planetary Science Letters*, *92*(2), 198–206.

Reekie, C., Jenner, F., Smythe, D., Hauri, E., Bullock, E., & Williams, H. (2019). Sulfide resorption during crustal ascent and degassing of oceanic plateau basalts. *Nature Communications*, *10*(1). https://doi.org/10.1038/s41467-018-08001-3

Regelous, M., Niu, Y., Wendt, J., Batiza, R., Greig, A., & Collerson, K. (1999). Variations in the geochemistry of magmatism on the East Pacific Rise at 10 Deg 30 N since 800 Ka. *Earth and Planetary Science Letters*, *168*, 45–63. https://doi.org/10.1016/S0012-821X(99)00048-5

Ridley, W., Perfit, M., Smith, M., & Fornari, D. (2006). Magmatic processes in developing oceanic crust revealed in a cumulate xenolith collected at the East Pacific Rise, 9 50′ N. *Geochemistry, Geophysics, Geosystems*, *7*(12). https://doi.org/10.1029/2006GC001316

Schiano, P., Birck, J.-L., & Allegre, C. (1997). Osmium-strontium-neodymium-lead isotopic covariations in mid-ocean ridge basalt glasses and the heterogeneity of the upper mantle. *Earth and Planetary Science Letters*, *150*(3–4), 363–379.

Sims, K. W., Blichert-toft, J., Fornari, D., Perfit, M., Goldstein, S., Johnston, P., et al. (2003). Aberrant youth: Chemical and isotopic constraints on the origin of off-axis lavas from the East Pacific Rise, 9–10 N. *Geochemistry, Geophysics, Geosystems*, *4*(10). https://doi.org/10.1029/2002GC000443

Sours-Page, R., Nielsen, R., & Batiza, R. (2002). Melt inclusions as indicators of parental magma diversity on the Northern East Pacific Rise. *Chemical Geology*, *183*, 237–261. https://doi.org/10.1016/S0009-2541(01)00384-9

Tang, M., McDonough, W., & Ash, R. (2017). Europium and strontium anomalies in the MORB source mantle. *Geochimica et Cosmochimica Acta*, *197*, 132–141.

Turner, S., Beier, C., Niu, Y., & Cook, C. (2011). U-Th-Ra disequilibria and the extent of off-axis volcanism across the East Pacific Rise at 9 30N, 10 30N, and 11 20N. *Geochemistry, Geophysics, Geosystems*, *12*(7), 1–18. https://doi.org/10.1029/2010gc003403

Wallace, P., & Carmichael, I. (1992). Sulfur in basaltic magmas. *Geochimica et Cosmochimica Acta*, *56*, 1863–1874. https://doi.org/10.1016/0016-7037(92)90316-B

Wanless, V. D., Perfit, M. R., Ridley, W. I., & Klein, E. M. (2010). Dacite petrogenesis on mid-ocean ridges: Evidence for oceanic crustal melting and assimilation. *Journal of Petrology*, *51*(12), 2377–2410. https://doi.org/10.1093/petrology/egq056

Waters, C. L., Sims, K. W. W., Soule, S. A., Blichert-Toft, J., Dunbar, N., Plank, T., et al. (2013). Recent volcanic accretion at 9 N–10 N East Pacific Rise as resolved by combined geochemical and geological observations. *Geochemistry, Geophysics, Geosystems*, *14*(8), 2547–2474. https://doi.org/10.1002/ggge.20134

Yi, W., Halliday, A., Alt, J., Lee, D., Rehkaemper, M., Garcia, M. O., et al. (2000). Cadmium, indium, tin, tellurium, and sulfur in oceanic basalts: Implications for chalcophile element fractionation in the Earth. *Journal of Geophysics Research*, *105*(B8), 18927–18948. https://doi.org/10.1029/2000jb900152

Zhang, Y., Meng, F., & Niu, Y. (2016). Hf isotope systematics of seamounts near the East Pacific Rise (EPR) and geodynamic implications. *Lithos*, *262*, 107–119.

Erratum

In the originally published version of this article, the supporting information tables were missing. The tables are now included in the supporting information. In addition, references to the tables in the article and in the Supporting Information S1 file have been modified from Tables 1-3 to Tables S1-S3. This may be considered the authoritative version of record.